https://doi.org/10.5194/essd-2026-194
Preprint. Discussion started: 4 May 2026

Open Access Earth System Science Data Discussions

High-resolution Digital Outcrop Dataset of a Fossil Hyperextended Rifted Margin, Swiss Alps

Leïla Morzelle[1], Peter Betlem[2], Geoffroy Mohn[1] and Julie Tugend[1]

[1]CY Cergy Paris Université, Sorbonne Université, CNRS-INSU, Institut des Sciences de la Terre de Paris, ISTeP, 1 rue Descartes, 95000 Neuville-sur-Oise, France
[2]NGI, Norwegian Geotechnical Institute, Sandakerveien 140, 0484 Oslo, Norway

Correspondence to: Leïla Morzelle (leila.morzelle@cuy.fr)

Abstract. Structure-from-motion (SfM) photogrammetry provides new possibilities for the interpretation of complex geological objects and settings through the digitalization of outcrops in the form of Digital Outcrop Models (DOMs). This study focuses on the acquisition, processing, and georeferencing of 12 DOMs targeting the Err and Bernina low-angle normal faults (LANFs) in the Central Alps. This area exceptionally preserves remnants of Jurassic rifting. Extensive Unmanned Aerial Vehicle (UAV) -based field campaigns (2022–2025) over 43 km², covering 1710 m elevation difference, combined with differential GNSS and regionally-available surface data, produced 12 high-resolution DOMs and associated products (point clouds, textured meshes (DOMs), tiled models, orthomosaics, and DEMs) with centimeter to decimeter resolution. A total of 15 control points per DOM were used to georeference and quality assure the digital data assets, 5 of which function as reference check points (CPs). Within the twelve DOMs, the total ground control points (GCPs) root mean square error (RMSE) ranges from 0.02 to 1.47 m and the RMSE of the CPs ranges from 0.49 to 3.11 m. Individual DOMs within the Fossil Alpine Tethys rifted margin DOM (FATDOM) Dataset reveal detailed internal fault structures, lithological variations, fracture networks, and tectono-sedimentary relationships, offering new insights into the architecture and kinematic evolution of LANFs that also extend to the seismic scale. Comparison of our DOMs with seismic data in present-day systems can be used to bridge the scale gap between local structural observations and regional interpretations. Beyond tectonic implications, the high resolution of our resulting DOMs enables a wide range of geoscientific applications including geomorphological studies focused on the monitoring of deglaciation. The data described in this paper are available on Zenodo under https://doi.org/10.5281/zenodo.18940068 (Morzelle et al., 2026).

1 Introduction

Structure-from-Motion (SfM) photogrammetry provides a robust and efficient solution for documenting complex geological environments (Betlem et al., 2024; Dering et al., 2019; James et al., 2019; Thiele et al., 2015). By reconstructing three-dimensional geometries from overlapping two-dimensional images, SfM allows the generation of spatially continuous, high-resolution, and accurately georeferenced digital outcrop models (DOMs), digital elevation models (DEMs), and orthomosaics. This approach is particularly suited to large, steep, and high-altitude outcrops where conventional surveying is impractical or unsafe, while preserving both geometric and textural information that can be quantitatively analyzed across a wide range of spatial scales (Burnham et al., 2024; Howell and Burnham, 2021).

The integration of multiple, spatially connected high-resolution DOMs enable systematic mapping of geological features, including bedding, folds, faults, and fracture networks, from the centimeter to the kilometer scale. In this sense, DOMs form a direct link between field-scale observations and seismic-scale interpretations, and are an important stepping stone to understanding geologically-complex extensional structures, including low angle normal faults (LANF) systems found in

https://doi.org/10.5194/essd-2026-194
Preprint. Discussion started: 4 May 2026

present-day, deep-water, rifted margins in the South China Sea (Legeay et al., 2024), Galicia margin (Lymer et al., 2019), West of Ireland (Lymer et al., 2023), Somalia margin (Sapin et al., 2021), and elsewhere.

Their characterization is essential for understanding extensional processes of the lithosphere (Buck, 1988; Collettini, 2011; Lecomte et al., 2012; Melosh, 1990; Wernicke, 1981) as well as for appraising resource potential in their associated sedimentary basins.

Past investigations have relied heavily on local field mapping and 2D panoramas, especially across the exposed fossil Alpine Tethys, a well-established onshore analogue system in the Swiss Alps with exceptionally well-preserved rift related LANFs (Epin and Manatschal, 2018; Froitzheim and Eberli, 1990; Manatschal, 2004; Mohn et al., 2012). Geological investigations in this region typically rely on conventional field methods and are strongly limited by accessibility, as many key structures in the Swiss Alps are in steep, remote, and frequently snow-covered terrain at elevations exceeding 2 500 m. In addition, ongoing erosion accelerated by climate change increasingly threatens the preservation of these sites. As a result, the digitization of this area (Figure 1) is of major interest to preserve the outcrops in a rapidly changing climate and provides new perspectives for understanding the formation processes of LANFs.

In this contribution we present the digitalization and integration of 12 DOMs in south-east Switzerland, capturing the Err and Bernina units in the distal part of the fossil hyper-extended Adriatic rifted margin as part of the initial release of the (regional) Fossil Alpine Tethys rifted margin DOM (FATDOM) dataset. Particular focus is given to the spatial resolution, georeferencing accuracy, overall data quality, geological integration, and FAIR data publishing (Wilkinson et al., 2016), ensuring that the data are findable, accessible, interoperable, and reusable for a wide range of future geological and geoscientific applications.

https://doi.org/10.5194/essd-2026-194
Preprint. Discussion started: 4 May 2026

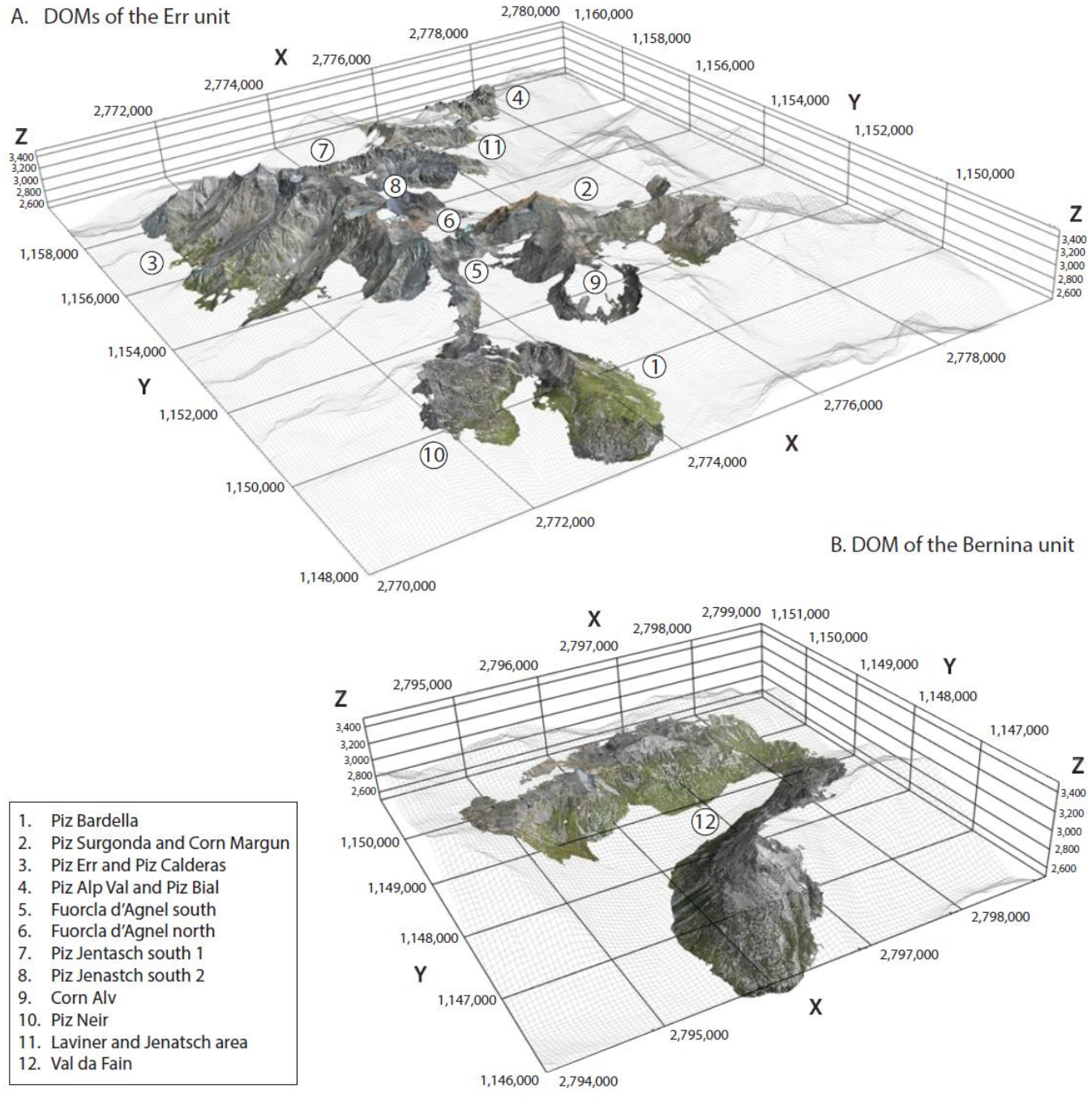

Figure 1: Spatial extent and visualization of the 12 digital outcrop models included in the initial release of the FATDOM dataset.

https://doi.org/10.5194/essd-2026-194
Preprint. Discussion started: 4 May 2026

2 Geological Setting

The southeastern Swiss Alps preserve a unique fossil example of a distal rifted margin formed during the opening of the Alpine Tethys (Froitzheim and Eberli, 1990; Manatschal and Nievergelt, 1997). This distal rifted margin belonged to the former Adriatic plate and was associated with extreme thinning of the continental crust and lithosphere during the Jurassic rifting.

Remnants of the distal Adriatic rifted margin in the Err and Bernina units are exceptionally preserved and extensively described in the literature (Froitzheim and Eberli 1990; Manatschal and Nievergelt 1997; Mohn et al. 2012; Manatschal et al. 2022). The Err and Bernina units, part of the lower Austroalpine nappes, are today included in an Alpine nappe stack with the Bernina unit overlying the Err unit (Froitzheim et al. 1994; Mohn et al. 2012; Ribes et al. 2019). These units exhibit low to mild Alpine overprint, including superimposed deformation and metamorphism (never exceeding greenschist facies conditions), while still preserving inherited rift-related structures (Ferreiro Mählmann 1995; Mohn et al. 2012; Ribes et al. 2019).

The units preserve former hyper-extended rift basins controlled by a well-developed succession of LANFs related to the Jurassic rifting (Figure 2) (Epin and Manatschal, 2018; Manatschal and Nievergelt, 1997; Masini et al., 2012). This LANF system controlled the stratigraphic architecture of syn-rift sediments and is linked to the formation of extensional allochthonous blocks derived from the hanging wall. These units consist of Paleozoic crystalline basement rocks, including granites and gneisses, overlain by Late Paleozoic to Mesozoic pre- and syn- and post-rift sediments (Epin and Manatschal, 2018; Ribes et al., 2019).

At least four sequential LANF systems have been identified across an area of more than 200 km² in this region: the Agnel, Jenatsch, Err, and Bernina LANFs (Figure 2) (Epin and Manatschal, 2018). These structures are included within the study area considered in this work (Figure 1).

https://doi.org/10.5194/essd-2026-194
Preprint. Discussion started: 4 May 2026

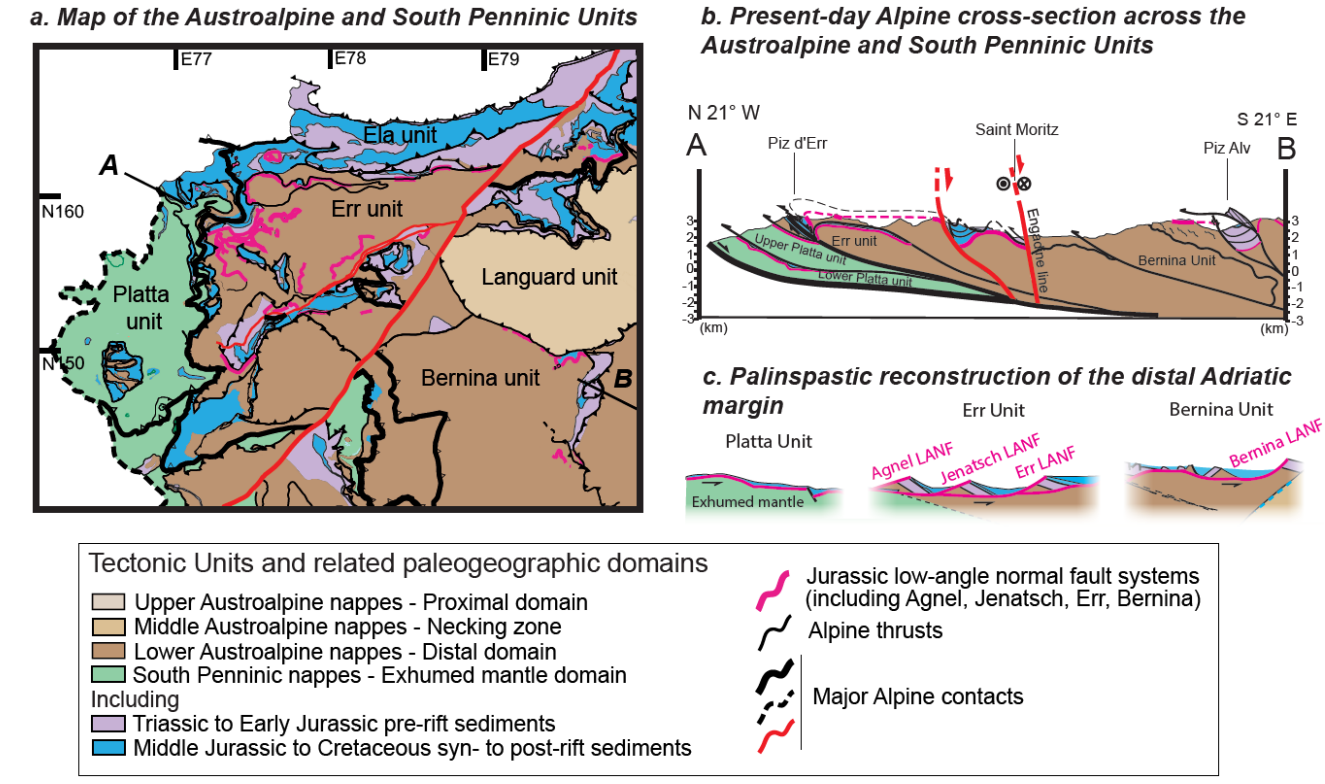

Figure 2: a) Simplified tectonic map along the Central Alps (eastern Switzerland), b) present-day alpine cross-section and c) palinsplastic reconstruction of the Adriatic margin, modified from Mohn et al. (2011), Mohn et al. (2012) and McCarthy et al. (2021).

3 Methods

Extensive Unmanned Aerial Vehicle (UAV) based field surveys enabled the acquisition of high-quality photogrammetric models suitable for the generation of DEMs, orthomosaics, and DOMs with centimeter- to decimeter-scale resolution. As described in detail below, the resulting products were quality assured and calibrated against existing regional reference datasets, to ensure accurate and consistent georeferencing.

3.1 UAV Surveying

We conducted four UAV summer data acquisition campaigns during 2022-2025. Three different UAV systems were used to acquire imagery (Table 1). During each survey, we conducted manual flight operations following the method described by Howell and Burnham, (2021) and lessons learned from the Svalbox data acquisition campaigns (Senger et al., 2021a; Betlem et al., 2023b, 2025). We opted for flights as perpendicular to the outcrops as terrain allowed while aiming for a constant UAV-to-outcrop distance, and we varied both flight altitude and camera angle for the various fly-bys. The UAV's image acquisition system was programmed to trigger automatically at intervals of 3 to 7 seconds, while manually re-focusing was done in between. Maximum fight speeds were adjusted based on imaging distance and acquisition conditions to ensure sufficient image

https://doi.org/10.5194/essd-2026-194
Preprint. Discussion started: 4 May 2026

overlap (>70%) while avoiding motion blur. An automatic white balance was used and ISO set to 100. Each outcrop was covered by between 1 and 13 flights, resulting in between 46 and 3045 images per model. The camera angles varied between 0° and -60°. Normalized, back-calculated UAV-to-outcrop distances are presented in Table 1 for each model, as are further survey details.

https://doi.org/10.5194/essd-2026-194
Preprint. Discussion started: 4 May 2026

Open Access Earth System Science Data Discussions

Table 1: Details of the photogrammetric data acquisition used to build the 12 DOMs of the FATDOM dataset.

Year	Day of data acquisition	Digital outcrop model	Orthomosaic	Drone and camera	Properties of camera	Number of flights	Number of aligned images / Total	Average flying altitude (m)	Coverage area (km)²	Distance camera/outcrop normalized
Field Campaign (FC) 2023	2023.08.07	Piz Bardella	1 	DJI Mavic 3 classic Hasselblad L2D-20c	12.29 mm focal length 20 MP images	3	487/488	372	2.57	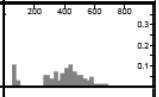
	2023.08.08	Piz Surgonda and Corn Margun	2 			6	972/973	318	6.84	
	2023.08.10	Piz d'Err and Piz Calderas	3 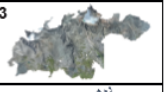			8	1131/1132	468	9.84	
	2023.08.11	Piz d'Alp Val and Piz Bial	4 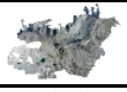			1	263	193	1.22	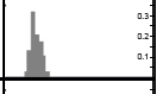
Field Campaign 2024	2024.09.10	Fuorcla d'Agnel south	5 	DJI Mavic 3 pro Hasselblad CMOS 4/3	24mm eq. f/2.8-f/11 20 MP	2	353	187	1.36	
		Fuorcla d'Agnel north	6 			2	332	196	1.37	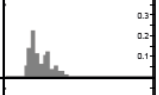
	2024.09.11	Piz Jenatsch south 1	7 			5	793	271	3.22	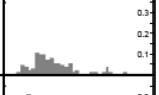
		Piz Jenatsch south 2	8 			1	46	199	0.615	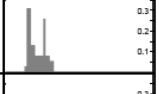
		Corn Alv	9 			1	219	261	1.78	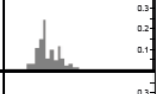
FC 2025	2025.07.18	Piz Neir	10 			4	498/499	177	2.30	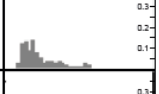
Merged Models	2022/2023	Laviner and Jenatsch area	11 	2022 DJI Mavic 2 pro Hasselblad L1D-20c / 2023 DJI Mavic 3 classic Hasselblad L2D-20c	2022 10.26mm focal length 20 MP images / 2023 12.29 mm focal length 20 MP images	13	3044/3045	124	4.08	
	2022/2023	Val da Fain	12 			12	1961	227	7.79	

https://doi.org/10.5194/essd-2026-194
Preprint. Discussion started: 4 May 2026

Open Access Earth System Science Data Discussions

3.2 Processing and quality control

The DOMs were reconstructed using the *Agisoft Metashape* (version 2.2.1 professional edition) commercial software. A summary and deviations from the workflow and processing parameters are provided below.

We used *Metashape*'s built-in image evaluation tool to estimate image quality, keeping images with qualities of 0.5 and above. Photos were aligned with highest accuracy and cameras optimized with the "exclude stationary tie points" setting enabled, facilitating scientific filtering of the tie points in subsequent steps. This resulted in sparse-point clouds containing between 330 020 and 16 063 436 points (Table 2) prior to filtering. The tie points were consecutively filtered by *Reconstruction Uncertainty*, *Projection Accuracy*, and *Reprojection Error*, each step followed by re-optimalisation of the camera positions. The details of the filtering steps are presented in Table 2.

We generated the dense-point clouds from depth maps, using the mild filtering criteria for the latter. No changes were made to the automatically generated bounding box. To improve overall quality, we filtered the dense point cloud by confidence: low quality points in the range 0-5 were removed. This decimated the dense-point clouds to between 23 611 731 and 361 543 706 points for the twelve DOMs of the dataset (Table 2). The mesh (model) was subsequently generated using the filtered dense cloud as input. Each model was filtered based on connected component size to remove unresolved and disconnected mesh elements, to further improve quality. Textures were generated for each model, and the models functioned as input for Tiled Models, the digital elevation models (DEMs), and orthomosaics.

Figure 1 uses the style Caption. The abbreviation "Fig." should be used when it appears in running text and should be followed by a number unless it comes at the beginning of a sentence (e.g. "The results are depicted in Fig. 5. Figure 9 reveals that."). Figures and tables as well as their captions must be inserted in the main text near the location of the first mention (not appended to the end of the manuscript). Regarding colour schemes, it is important that your maps and charts allow readers with colour vision deficiencies to correctly interpret your findings. Please check your figures using the Coblis – Color Blindness Simulator and revise the colour schemes accordingly.

3.3 Georeferencing: GCPs and CPs procedures

Accurate georeferencing of the DOMs was ensured through use of Post-Processing Kinematic (PPK) data (only for models 11; see Betlem et al., (2023a); and 12) and natural markers, implemented prior to tie-point filtering as ground control (GCPs) and check points (CPs). All data were set to the Swiss national CH1903+/LV95 (EPSG:2056) projection. Natural markers

https://doi.org/10.5194/essd-2026-194
Preprint. Discussion started: 4 May 2026

were strategically chosen within the area through integration of the SwissALTI3D DEM, which has a resolution of 0.5 m (Swisstopo 2022a), and the orthomosaic of SwissDOP10 with a ground resolution of 0.25 m in the alpine part of the country (Swisstopo, 2022b). The SwissALTI3D dataset is based on LIDAR data and the SwissIMAGE dataset is based on imagery data, both acquired by aerial surveys.

Up to 15 markers were picked per model, including for the model 11 integrated from Betlem et al., (2023a) for which PPK data is available. Up to 10 markers were used as GCPs for georeferencing of the data and up to 5 were used as CPs, to quantify the total error independently. Mean and root-mean-square errors (RMSEs) were calculated for both the GCPs and CPs, and further details are described in Table 3 and appendices (Tables A1-A13).

Table 3 presents the details of GCPs and CPs used for the georeferencing of all the DOMs of the dataset. Within the twelve DOMs, the total GCPs RMSE ranges from 0.02 to 1.47 m. The RMSE of the CPs ranges from 0.49 to 3.11 m.

https://doi.org/10.5194/essd-2026-194
Preprint. Discussion started: 4 May 2026

Open Access Earth System Science Data Discussions

Table 2: Details of the image alignment and camera optimization steps, including the filtering steps of the spare cloud as processed in Agisoft Metashape. RU: reconstruction uncertainty (specific filtering level for each model); PA: projection accuracy (all models applied a filtering level of 2); RE: reprojection error (all models applied a filtering level of 0.3).

Digital outcrop model	Orthomosaic	Number of camera stations	Tie points (points)	Sparse cloud (points)	Sparse cloud processing				Point cloud (points)
					Reconstruction Uncertainty (RU) filter	Tie points after RU filtering (points)	Tie points after PA filtering level 2 (points)	Tie points after RE filtering level 0.3 (points)	
Piz Bardella	1 	487	2 948 069	2 509 846	16.9	1 260 779	688 304	411 122	61 733 128
Piz Surgonda and Corn Margun	2 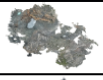	972	5 959 954	5 081 064	16.3	2 547 458	2 069 072	751 066	142 807 073
Piz d' Err and Piz calderas	3 	1131	6 137 462	4 839 198	21.3	2 428 992	1 982 305	755 843	140 991 948
Piz d'Alp Val and Piz Bial	4 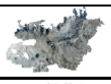	263	1 796 414	1 453 836	17.9	730 886	563 405	235 908	55 666 625
Fuorcla d'Agnel south	5 	353	2 314 980	1 982 114	15.7	995 408	905 872	371 269	99 840 196
Fuorcla d'Agnel north	6 	325	2 156 717	1 771 574	18	885 970	819 328	377 024	115 280 732
Piz Jenatsch south 1	7 	793	4 781 033	3 685 379	20.4	1 850 806	1 611 743	857 483	143 421 685
Piz Jenatsch south 2	8 	46	357 673	330 020	15.3	166 385	148 525	83 221	23 707 599
Corn Alv	9 	219	1 351 763	1 064 432	24.1	533 078	487 216	231 801	43 986 810
Piz Neir	10 	498	3 018 458	2 183 546	15.7	1 092 294	953 842	575 242	121 082 062
Laviner and Jenatsch area	11 	3044	19 840 830	16 063 436	15.8	8 034 683	5 655 847	2 417 141	361 543 706
Val da Fain	12 	1957	12 721 380	10 778 369	15.4	5 423 320	4 368 807	2 143 060	334 858 976

https://doi.org/10.5194/essd-2026-194
Preprint. Discussion started: 4 May 2026

Open Access Earth System Science Data Discussions

Table 3: Details of the ground control points (GCP) and check points (CP) used for the georeferencing and the RMSE.

Digital outcrop model	Orthomosaic	GCPs and CPs RMSE (X – Easting, Y – Northing, Z – Altitude)							
		Type	Count	X e. (cm)	Y e. (cm)	Z e. (cm)	XY e. (cm)	Total (m)	Total (pix)
Piz Bardella	1 	GCP	10	38.6	55.1	29.0	67.3	**0.733**	**1.40**
		CP	5	103.7	32.9	62.7	108.7	**1.256**	**1.56**
Piz Surgonda and Corn Margun	2 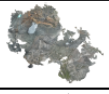	GCP	10	0.6	1.1	0.8	1.2	**1.473**	**1.41**
		CP	5	42.9	18.3	91.6	46.7	**1.028**	**1.23**
Piz d' Err and Piz Calderas	3 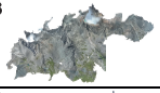	GCP	10	0.5	0.3	0.4	0.6	**0.721**	**0.96**
		CP	5	160.6	181.8	194.9	242.6	**3.111**	**3.47**
Piz d'Alp Val and Piz Bial	4 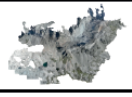	GCP	10	1.4	1.4	1.1	2.0	**0.022**	**1.79**
		CP	5	67.6	10.1	11.7	121.8	**1.689**	**1.53**
Fuorcla d'Agnel south	5 	GCP	10	0.6	0.8	1.3	1.0	**0.017**	**1.88**
		CP	5	107.6	138.3	160.5	175.2	**2.376**	**1.28**
Fuorcla d'Agnel north	6 	GCP	10	1.5	1.9	2.7	2.4	**0.036**	**1.84**
		CP	5	192.8	74.6	221.7	206.8	**3.031**	**2.64**
Piz Jenatsch south 1	7 	GCP	10	0.8	1.1	1.5	1.4	**0.020**	**1.41**
		CP	5	33.3	17.6	31.6	37.7	**0.492**	**1.07**
Piz Jenatsch south 2	8 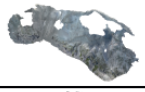	GCP	7	0.8	0.7	1.3	1.0	**0.016**	**1.79**
		CP	3	23.6	37.2	79.5	44.1	**0.909**	**0.88**
Corn Alv	9 	GCP	10	0.7	1.0	1.2	1.3	**0.017**	**1.13**
		CP	5	59.2	57.1	70.8	82.2	**1.085**	**1.35**
Piz Neir	10 	GCP	10	0.9	1.1	1.7	1.5	**0.220**	**1.45**
		CP	5	26.9	42.0	49.9	49.9	**0.705**	**1.23**
Laviner and Jenatsch area	11 	GCP	10	22.6	26.7	50.8	35.0	**0.617**	**1.13**
		CP	5	94.7	37.3	55.7	101.7	**1.160**	**1.18**
Val da Fain	12 	GCP	10	2.7	4.2	1.0	5.0	**0.051**	**1.07**
		CP	5	37.4	20.7	31.0	42.8	**0.528**	**0.82**

https://doi.org/10.5194/essd-2026-194
Preprint. Discussion started: 4 May 2026

Open Access Earth System Science Data Discussions

4 Results

Processing of the dense cloud enabled the generation of DOMs and orthomosaics with a ground resolution ranging from 5 to 15.4 cm/pixel and DEMs with a resolution ranging from 10 to 30.9 cm/pix (Table 4). The 12 reconstructed DOMs cover an area of 43 km². For each model a composite figure consisting of 6 charts is used to facilitate quality control. In the summary below, references to Figure 3 are provided for illustration purposes, with similar charts for the other models available in the Appendices A1-A11.

Table 4: Product details for each model of the FATDOM dataset.

Digital outcrop model	Orthomosaic	RSM reprojection error (m (pix))	Max reprojection error (m (pix))	Dense cloud point density (#/m²)	Dense cloud point confidence (mean/m²)	Model (vertices)	DEM point density (pts/m²)	DEM resolution (cm/pix)	DEM Elevation (m)	Orthomosaic resolution (cm/pix)
Piz Bardella	1 	0.144 (0.302)	0.988 (2.883)	Min: 1 Max: 275	Min: 6 Max: 71.16	5 734 759	21.7	21.5	2040 - 2850	10.7
Piz Surgonda and Corn Margun	2 	0.151 (0.218)	1.759 (3.321)	Min: 1 Max: 538	Min: 6 Max: 148.96	16 657 878	21.2	21.7	2550 - 3200	10.9
Piz Err and Piz calderas	3 	0.150 (0.213)	2.041 (3.290)	Min: 1 Max: 410	Min: 6 Max: 174.32	20 732 633	10.5	30.9	2200 - 3400	15.4
Piz d'Alp Val and Piz Bial	4 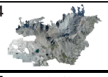	0.148 (0.217)	1.266 (1.830)	Min: 1 Max: 1079	Min: 6 Max: 84.10	10 649 377	53.3	13.7	2630 - 3070	6.85
Fuorcla d'Agnel south	5 	0.152 (0.203)	1.282 (2.448)	Min: 1 Max: 1425	Min: 6 Max: 35.98	10 672 909	69.8	12	2640 - 3210	5.98
Fuorcla d'Agnel north	6 	0.151 (0.198)	3.051 (6.357)	Min: 1 Max: 1244	Min: 6 Max:42.79	13 160 704	60.4	12.9	2760 - 3340	6.44
Piz Jenatsch south 1	7 	0.143 (0.187)	1.934 (3.284)	Min: 1 Max: 1217	Min: 6 Max: 88.19	19 532 179	33.2	17.3	2580 - 3400	8.67
Piz Jenatsch south 2	8 	0.146 (0.194)	1.269 (1.864)	Min: 1 Max: 1405	Min: 6 Max: 16.28	2 755 317	59.5	13	2710 - 3040	6.48
Corn Alv	9 	0.145 (0.190)	0.894 (1.466)	Min: 1 Max: 1294	Min: 6 Max: 67.45	5 438 851	30.8	18	2510 - 3010	9
Piz Neir	10 	0.141 (0.192)	1.617 (2.793)	Min: 1 Max: 1257	Min: 6 Max: 70.28	16 637 387	49.2	14.3	2330 - 2910	7.13
Laviner and Jenatsch area	11 	0.145 (0.214)	1.529 (4.197)	Min: 1 Max: 633	Min: 6 Max: 14.21	8 752 118	100	10	2700 - 3750	5
Val da Fain	12 	0.146 (0.208)	1.329 (2.328)	Min: 1 Max: 757	Min: 6 Max: 80.78	4 928 564	35.7	16.7	2130 - 3030	8.36

https://doi.org/10.5194/essd-2026-194
Preprint. Discussion started: 4 May 2026

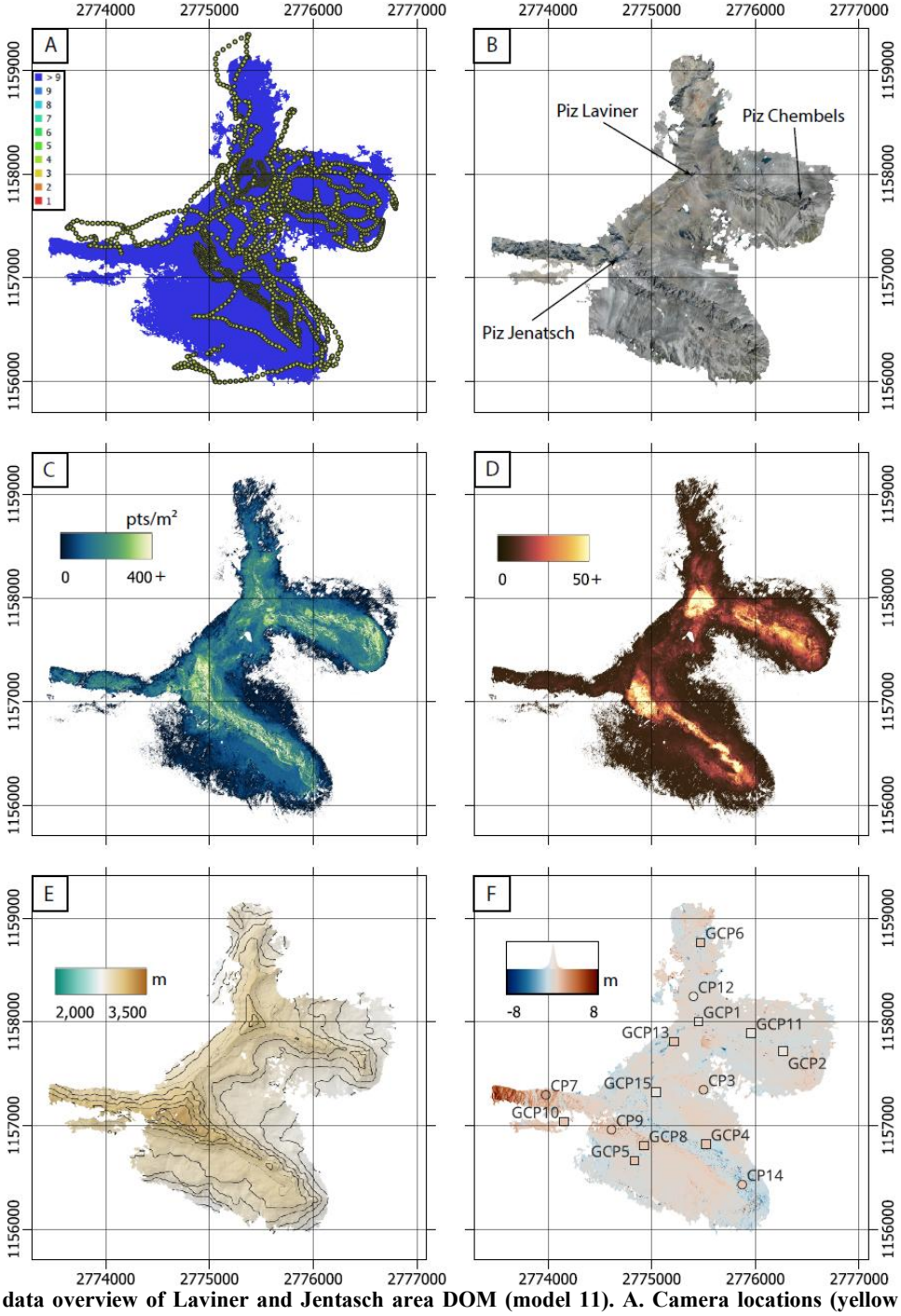

Figure 3: Detailed data overview of Laviner and Jentasch area DOM (model 11). A. Camera locations (yellow dots) and image overlap indicate good coverage with a majority covered by at least 9 images. B. The Orthomosaic has a spatial resolution of 5 cm/pix. C. The density of the dense cloud ranges from 0 to ≥400 points/m², lower in the periphery and highest in the center of the model and in steep slopes. D. The confidence, average of all points over a square meter, of the dense cloud ranges from 0 to ≥50. E. The Digital Elevation Model (DEM) presents elevation values ranging from 2 680 m to 3 250 m, has a spatial resolution of 10 cm/pixels. F. The DEM comparison map shows the difference between the DEM and regional reference SwissALTI3D DEM.

https://doi.org/10.5194/essd-2026-194
Preprint. Discussion started: 4 May 2026

4.1 Processing of the datasets

The A chart in each figure shows the camera positions and overlap during the different flights (Figures 3 and A1 to A11). Across all DOMs, image overlap consistently shows that the mapped area was generally covered by at least nine images. Models 1, 2, 3, 10, and 12 were almost fully covered by 9 or more images (Figures A1, A2, A3, A10 and A11). Localized deviations occur in a few DOMs, where peripheral or central sectors receive fewer images (minimum coverage ranging from 1 to 5 images). Model 4 shows mostly more than 9-image coverage, with a small western sector covered by 5 images (Figure A4). Models 5 and 7 show central areas with reduced coverage (≥1 image) (Figures A5 and A7), models 6 and 8 present limited peripheral areas with only 2 images of overlap (Figures A6 and A8). Model 9 is mostly covered by more than 9 images, except for a small eastern area covered by 5 images (Figure A9).

Normalized, back-calculated UAV-to-outcrop distances are presented in Table 1 for each model. More significant variations are observed for datasets incorporating multiple flights. For example, the distance between the camera and the outcrops varies between 139.83 and 318.35 m for model 4 based on one flight, versus between 60.99 and 1 141.33 m for model 2, whose data was acquired during six flights (Table 1).

The C chart in each figure shows the density of the dense cloud (Figures 3 and A1 to A11). The maximum density of the points in the generated point clouds varies depending on the model (Table 4). It ranges from 275 points/m² for model 1 (Figure A1), to 1425 points/m² for model 5 (Figure A5). Often the density is lower in the periphery and highest in areas with outcrop of geological interest, as well as in areas with steep inclines (e.g., Figure 3), owing to how the calculation is made per horizontal square meter.

The D chart in each figure presents the average confidence per m² of the dense point cloud (Figures 3 and A1 to A11). These values range from a minimum of 6 for all models, to maxima in the range of 16.28-148.94 (Table 4). The minimum corresponds to the level of filtration of 5 used during the processing on *Agisoft metashape* (see Methods). Both the highest density and confidence of the dense cloud appear to overlap, either near the center of the models or in close proximity to areas of interest (e.g., model 1; Figure A1) such as along exposed (vertical) outcrops and ridges (e.g., model 11; Figure 3). The lowest confidences are observed at the periphery of the study area in regions with poorer coverage at the time of acquisition, as also evident from the reduced point density and camera overlaps (e.g., model 1; Figure A1).

4.2 Orthomosaics and DEMs

The B chart in each figure presents the orthomosaic of the models (Figures 3 and A1 to A11). Model 11 presents a high resolution with 5 cm/pix (Table 4). The models 4, 5, 6 and 8, characterized by a low number of flights and small geographical

https://doi.org/10.5194/essd-2026-194
Preprint. Discussion started: 4 May 2026

areas (Table 1) also have a high resolution ranging from 5.98 to 6.85 cm/pix (Table 4). Models 1, 2 and 3 have lower resolutions ranging from 10.7 to 15.4 cm/pix (Table 4). Models 7, 9, 10 and 12 show resolutions ranging from 7.13 to 9 cm/pix (Table 4).

The E chart in each figure shows the DEMs (Figures 3 and A1 to A11). They range in elevation from 2 130 to 3 400 m with a resolution of 10 to 30.9 cm/pix (Table 4).

4.3 Quality control of the datasets

Quality was ensured through manual inspection and (internal) error analysis. Available regional SwissALTI3D DEM and SwissIMAGE orthomosaic data further facilitates detailed comparison with the generated data products, including model wide and localized DEM differences, and changes in terrain information. The F chart in each figure shows the DEM comparison map based on the reference SwissALTI3D DEM and the histogram of deviation distribution (Figures 3 and A1 to A11). The difference in elevation between the two datasets generally follows a normal distribution set at around 0 m (as illustrated for model 11; Figure 3F). Overall, discrepancies mostly range between -1 and +1 m.

The largest elevation deviations are generally observed at the periphery of the models. Elsewhere, localized, negative deviations are found for the model 2 and 3 DEM comparison (Figures A2 and A3), showing values between -4.5 and -2 m, while comparison of model 7 exhibits stronger negative deviations ranging from -6.5 to -3 m across glaciated terrain (Figure A7). Negative deviations are also observed over lakes, notably in model 4 (approximately -2.5 m) (Figure A4), a pattern that persists in model 5 where lake-related differences reach values as low as -1.75 m (Figure A5). In contrast, positive deviations are locally found where snow patches can be seen in the orthomosaic, for example in model 7 where values around +3 m correspond to isolated snow-covered areas (Figure A7). Additional, localized discrepancies occur near anti-avalanche structures (model 1) (Figure A1), on valley floors (models 3 and 7; Figures A3 and A7), and at the lowest points of some models. Several DOMs (model 6, 8, 9, 10, 11, and 12; Figures 3, A6, A8, A9, A10 and A11) are characterized by positive deviations in areas prone to erosion and gravitational instability, such as in and below steep slopes, a pattern that becomes more extensive in models 9 and 10 (Figures A9 and A10). Finally, model 9 shows large areas in the east covered from a greater distance (Figure A9), as does model 4 in the southwestern part, contributing to significant negative deviations (Figure A4).

4.4 Geological observations and DOM overlap

The present-day landscape of the Err unit is characterized by numerous peaks above 3 000 m, including well-exposed glaciers such as the Vadret Traunter Ovas glacier in model 2 and the Vadret d'Err glacier in model 7 (Figure 4A).

Geologically, the Err unit (Figure 4A) is subdivided from south to north into several structural domains separated by major tectonic contacts. Models 1, 5, 9 and 10 capture it in the southern part, where extensional allochthonous blocks composed of pre-rift and syn-rift sediments directly overlie a Permian basin. These DOMs capture the Piz Bardella/Corn Alv extensional

https://doi.org/10.5194/essd-2026-194
Preprint. Discussion started: 4 May 2026

allochthon, which is a breakaway block accommodating the termination of the Jenatsch LANF and the initiation of the Agnel LANF (Epin and Manatschal, 2018). The transition between the southern and northern parts of the Err unit is captured by models 2 and 6, corresponding to the northern limit of the Permian basin. In the northern part of the Err unit, models 3, 4, 7, 8, and 11 capture the Paleozoic basement with preserved extensional allochthons related to LANFs. This area records several thrust faults within the Err unit, as also captured by models 3 and 8. Across the northern part, model 11 captures the interactions between the Jenatsch and Err LANFs.

Model 12, acquired in the Bernina unit (Figure 4B), preserves a major recumbent fold related to a thrust fault at Piz Alv and Piz Tschüffer, representing a former extensional allochthonous block (Mohn et al. 2012). Further to the north-west, the Bernina LANF is observed at the top of the Paleozoic basement. It documents a substantial assemblage of extensional allochthonous blocks of pre-rift sediments of variable size ranging from several meters to hundreds of meters overlain by syn-rift sediments (near Cho dal Fain).

https://doi.org/10.5194/essd-2026-194
Preprint. Discussion started: 4 May 2026

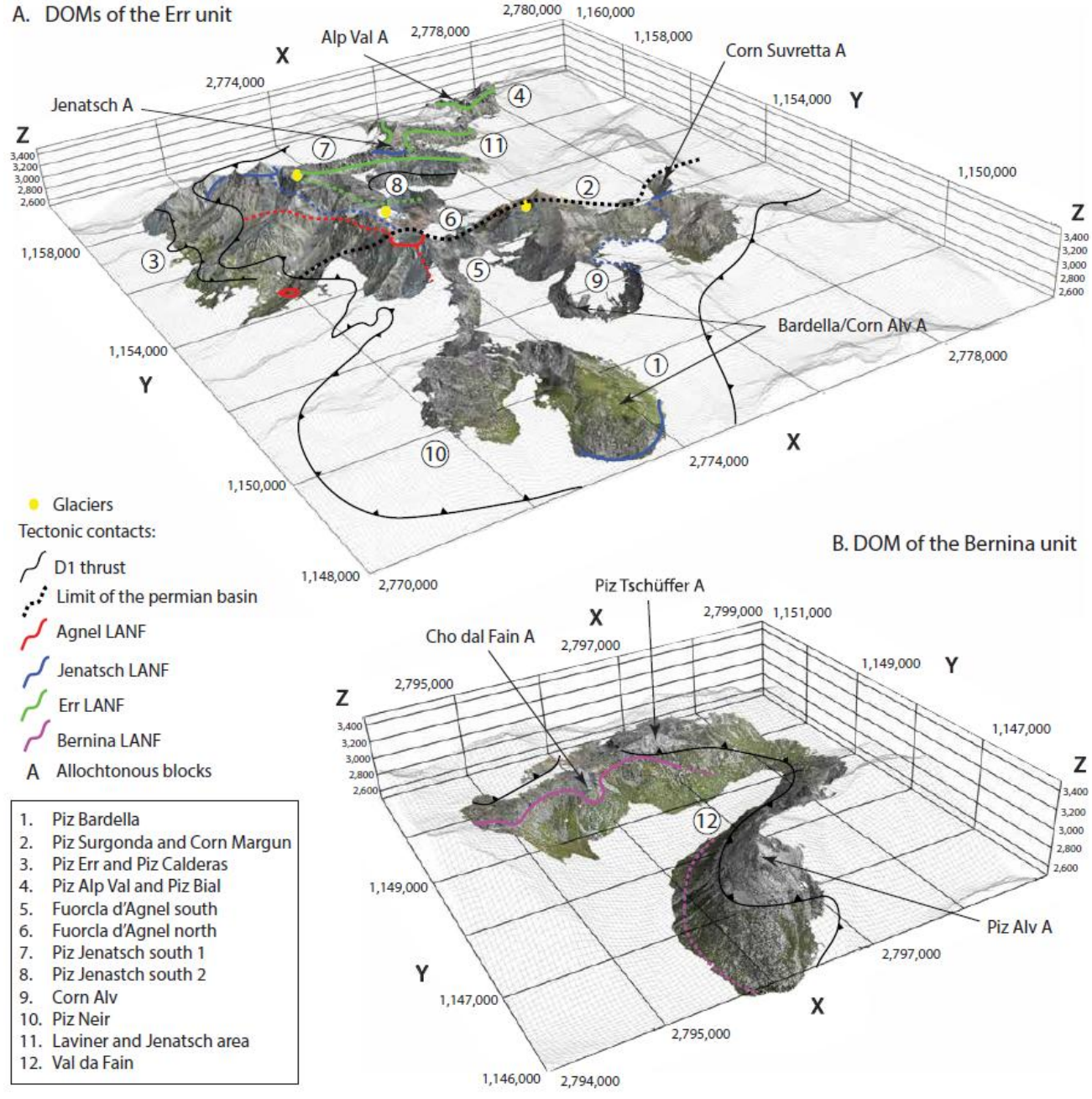

Figure 4: Visualization of the major tectonic contacts in the 12 digital outcrop models of the Err and Bernina units. The tectonic contacts are modified from Epin and Manatcshal (2018).

255

https://doi.org/10.5194/essd-2026-194
Preprint. Discussion started: 4 May 2026

5 Discussion

The data quality within the dataset varies depending on the acquisition choices and constraints, landscape specificities, and data processing parameters. Data quality is discussed and compared with the Swisstopo reference datasets (Swisstopo, 2022a, b). When combined with local geoscientific datasets and field observations, the quantifiable data form tool suited for integrated and detailed studies ranging from the area scale (~kms) to the outcrop scale (km-cm). The resulting 3D coverage provides several potential applications concerning the geological interpretation of the LANFs in a fossil distal margin, comparison with seismic data from present-day rifted margins, and glacier evolution.

5.1 Data quality

5.1.1 Georeferencing quality and selection of GCPs and CPs

Georeferencing was carried out by manually selecting control points (GCPs and CPs, Table 3) corresponding to easily identifiable, robust and stable surface features such as the CP4 in model 9 with an error in xyz of 0.21 m (Table B9). While this approach provides satisfactory results, the acquisition workflow can be further improved and georeferencing errors reduced during data processing by using artificial ground targets or differential GNSS measurements. However, the implementation of such methods remains challenging due to the very large spatial extent of the study area.

Within the individual models, the quality and reliability of both GCPs and CPs vary depending on the nature and location of the features selected by the operator. Particular attention was given to avoiding control points located in areas subject to seasonal or short-term surface changes, such as lakes, glaciers, moraines, or snow-covered zones or anthropogenic features, such as buildings. For instance, features such as manmade constructions (model 12, Figure A11) were avoided where differences were observed between acquisition periods. In addition, glacier-covered areas present in Models 2, 3, and 7 (Figures A2, A3, A7) with ice dynamics and retreat were also avoided, as substantial temporal variability can affect the overall georeferencing accuracies.

Despite these precautions, some control points display reduced reliability because they may have been affected by active geomorphic processes, including erosion or rock displacement, especially on steep slopes or scree slopes, where local displacements are likely. This is illustrated by CP7 and CP14 in model 11 (Table B11), which exhibit relatively high xyz errors of 1.89 m and 1.43 m, respectively, with an average xyz error of 1.16 m for all CPs versus 0.60 m when these are excluded. Similar observations can be made for the CP4 (model 3, xyz error of 3.91 m, see Table B3), which was picked as the edge of a boulder. In addition, the selection of control points located near the periphery of the models was avoided as much as possible, as these areas are more prone to distortion effects. Such distortions are illustrated by, for example, GCP8 in model 1 (xyz error of 1.50 m versus 0.73 m for all, Table B1) and by CP11 in model 3 (xyz error of 4.66), which sits in part of the model not adequately covered by close-proximity imagery despite having sufficient camera overlap (Figure A3).

https://doi.org/10.5194/essd-2026-194
Preprint. Discussion started: 4 May 2026

Overall, the georeferencing protocol applied in this study yields total GCP RMSE ranging from 0.02 (model 9) to 1.47 m (model 2) (Table 3). Because GCPs constrain the internal georeferencing of each model, their RMSE primarily reflects model distortion and intrinsic reconstruction quality. In contrast, CP RMSE values, which range from 0.49 (model 7) to 3.11 m (model 3) (Table 3), provide an estimate of the absolute georeferencing accuracy in geographic space. These metric error values are of the same order of magnitude as those typically obtained from UAV surveys equipped with RTK-GNSS systems (James et al., 2019).

5.1.2 Comparison with available regional data

The reported GCPs, CPs and DEMs errors must also be interpreted in light of the intrinsic accuracy of the reference datasets (i.e. Swisstopo elevation and planimetric data) used for georeferencing. The reference dataset used to calibrate our DOMs is composed of the SwissALTI3D DEM (Swisstopo, 2022a) and the SwissDOP10 orthomosaic (Swisstopo, 2022b) which shows both technical and seasonal differences compared to the dataset we acquired. The absolute positional accuracy of Swisstopo dataset typically corresponds to a decimetric scale depending on data type, terrain complexity, and acquisition method. The accuracy of swissALTI3D varies depending on the source data and input methods. Average deviations after manual updates range from 25 cm to 1 m (Swisstopo, 2022a). The planimetric accuracy of the SWISSIMAGE dataset is between +/-0.1 and +/-0.25 m (Swisstopo, 2022b). For the DEM of the study area, above 2 000 m the error is +/-1 m and +/-50 cm below 2 000 m; and for the Orthomosaic the error is +/-0.25 m in the alpine environment.

The Swisstopo dataset was acquired during aerial surveys in the Alps at an altitude of approximately 6 000 meters, with a ground resolution of 25 cm/pix for the orthomosaics (Swisstopo, 2022b) and a resolution of 50 cm/pix for the DEM of SwissALTI3D (Swisstopo, 2022a). The orthomosaics resolution of the FATDOM dataset ranges from 5 to 15.4 cm/pix and the DEMs resolution ranges from 10 to 30.9 cm/pix. The centimeter to decimeter resolution of the DOMs in the FATDOM dataset is therefore up to one order of magnitude better than that of the reference dataset, which has implications for the comparison between both data sets. Similar magnitude differences are observed in the associated errors (centimetric for FATDOM, decimetric for Swisstopo) that must also be accounted for when comparing the data and addressing inconsistencies between the two.

Consequently, residual errors below approximately +/-1 m may not necessarily reflect true inaccuracies of our DOMs, but rather the limited precision of the reference data itself. At this scale, part of the measured misfit likely reflects limited accuracy and precision of the reference dataset in resolving small spatial variations rather than systematic errors introduced during the georeferencing process. This is particularly relevant in high-relief alpine environments, where steep slopes and surface roughness further reduce the effective accuracy of reference DEMs (Swisstopo, 2022a). This is particularly relevant for small-

https://doi.org/10.5194/essd-2026-194
Preprint. Discussion started: 4 May 2026

scale features (e.g., rocks smaller than 0.5 m), which may be unresolved in the Swisstopo dataset but are clearly captured by the higher resolution of some our UAV data.

The comparison of our dataset with the reference dataset highlights systemic (local) mismatches and errors that are predominantly located in steep slopes, cliffs, moraines, scree slopes, glaciers, and in areas affected by human activity (e.g., buildings, fences). The observed mismatches between the two datasets can be important (several meters) in some DOMs, especially those with high reliefs and steep peaks such as models 3, 8 and 11 (Figure A3, A8 and 3). For example, model 11 images Piz Jenatsch with a summit at 3 251 m and east-west ridges bordered by steep cliffs where a mismatch of 8 meters is observed. A possible explanation is the different modes of acquisition. Swisstopo data were acquired by an aircraft that flew parallel to the ground, which may result in insufficient data across covered, steep terrain and cliffs. This is contrasted by the UAV method of acquisition which allows for unhindered access to such terrain and thus affords better resolution across such areas. This may account for some of the differences observed in models of steep slopes.

Other mismatches can be associated with the constant evolution of the landscape in such Alpine terrain. Models 3 and 7 (Figures A3 and A7) both capture moraines and glaciers in areas where the DEM comparison shows a significant mismatch of up to several meters. Such mismatches are expected as the Swisstopo dataset was neither acquired during the same year nor during the same season as our DOMs. Therefore, variations of the morphology and volume of the moraines and glaciers are expected and may be used for time series terrain analysis (see section 5.2).

From a geological perspective, the magnitude and spatial distribution of the georeferencing errors are on the meter scale (Table 3). This range is suitable for spatial analyses at the regional kilometric scales considered in this study. The observed error levels of each DOMs remain small (around 0) compared to the characteristic dimensions of the geological features investigated. The absence of a gradient in the DEM comparison plots (charts F, Figures 3, A1-A11) suggests there is no systematic tilt, though local tilting may occur in the periphery and beyond the key outcrops of interest. Therefore, the residual georeferencing uncertainties are negligible with respect to the size of major tectonic structures targeted for digitalisation. This allows the correlation of the geological structures on adjacent DOMs such as LANFs and thrust systems, as for example with the Err LANF, mapped across adjacent models 3, 7, and 11 (Figure 7).

5.1.3 Quality variations and limitations of the datasets

Some DOMs exhibit higher spatial resolution than others. For instance, model 11 has a ground resolution of 5 cm/pixel compared to model 3 that only has a resolution of 15.4 cm/pixel (Table 4). This can be explained by the acquisition of 3 045 images and 13 flights to cover an area of 4.08 km² for model 11 while model 3 is only based on 1 132 images and 8 flights acquired over a much larger area of 9.84 km² (Table 1).

https://doi.org/10.5194/essd-2026-194
Preprint. Discussion started: 4 May 2026

The DOMs exhibit minor gaps across the datasets as a result of a heterogenous data coverage with typically less images near the model edges, in contrast to a higher density of images for first order geological structures (i.e., structures of interest). Blurred areas appear in recesses, and local distortions are particularly noticeable at the model peripheries where image availability and overlap are insufficient (e.g., see model 5; Figure A5). This may be due to manually operated UAV flights. However, the significant topographic variations in the study area (approximately 840 m of elevation difference within the dataset) and operational constraints prevented the acquisition of images through pre-planned autonomous missions. In addition, the observed distortions (e.g. image stretching, blurring, and erroneously textured domains), particularly observed in the periphery, correspond to extrapolated areas during the processing (e.g., see model 8; Figure A8).

Textureless domains are visible along ridges and steep peaks and correspond to artifacts generated during reconstruction in *Agisoft Metashape*. Variations in cloud cover, causing shadows and changes in lighting, can also reduce the quality of the model, as also observed in the color discontinuities between and within different DOMs, such as in model 12 (Figure A11). The differences must be minor so they cannot be interpreted as geological structures or variations in lithology. In the FATDOM dataset, color or texture variations remain spatially limited. Therefore, the risk of confusion by different interpreters is small, for example for the interpretation of distinct lithologies (basement versus sedimentary rocks) or for the regional interpretation of tectonic contacts (LANFs, see for e.g. model 11, Figure 3; Alpine thrusts, see for e.g. model 3, Figure A3).

The spatial resolution of the DEMs is two times lower than that of the DOMs and orthomosaics, due to processing choices implemented in the photogrammetric workflow : the DEMs were interpolated from the 3D model because the model was filtered (see Methods). The vertical accuracy is lower than the horizontal accuracy, which is consistent with the geometric characteristics of SfM photogrammetry. Planimetric coordinates are generally better constrained by image overlap and tie-point distribution, whereas elevation estimates are more sensitive to image matching uncertainties, camera calibration errors, and intersection geometry. This anisotropic error distribution has been widely documented in UAV-based SfM surveys (Gindraux et al., 2017; James et al., 2019).

At the outcrop scale, the internal consistency of individual models, together with the generally low and spatially coherent CP errors (Tables A1-A12), ensures that relative measurements such as distances, orientations, and structural relationships are geologically useful, for the investigation of fracture networks and brittle deformation patterns for example.
As a result, both intra-model analyses and the combined interpretation of multiple models are well suited for geological interpretation, provided that measurements are interpreted within the known bounds of the georeferencing uncertainty

https://doi.org/10.5194/essd-2026-194
Preprint. Discussion started: 4 May 2026

5.2 Comparison with other DOM datasets

The literature presents numerous DOMs acquired in the Alps at the outcrop to cliff scale (typically a few square kilometers). In these studies, the integration of field observations and DOMs is commonly used to support geological interpretations, notably for the characterization of fault zones (Bistacchi et al., 2015; Manna et al., 2023), fracture network analysis (Binda et al., 2021), and slope instability and hazard assessment (Menegoni et al., 2020). These studies generally rely on centimetric-resolution DOMs, which are comparable to the spatial resolution achieved in the FATDOM dataset. This resolution is one of several key criteria for DOM quality, as it controls the ability to accurately identify and measure small-scale geological structures such as fractures, fault planes, and stratigraphic features. The FATDOM differs from previously published Alpine models by its larger surface extent and by its applicability across a wide range of geological processes, from landscape to tectonic evolution spanning rifting to orogenic phases.

Beyond resolution, the quality of DOM datasets and availability can also be assessed in terms of spatial extent, number of individual models, georeferencing quality, and data accessibility. Although several global online databases of DOMs exist, including V3Geo (Buckley et al., 2022) and e-Rock (Cawood and Bond, 2019), most of them do not provide open access to raw input data, processing documentation, or the DOM products themselves for reuse (see discussion in Betlem et al., 2023b). Another example is SafariDB, which is reserved for industry and offers more than 800 virtual outcrops (www.safaridb.com). Such limitations conflict with the FAIR principles (findable, accessible, interoperable, and reusable) (Wilkinson et al., 2016), since full and open availability of the complete dataset (particularly the input data) is crucial for reprocessing models and reassessing earlier interpretations. These aspects are widely recognized as fundamental priorities for future research (Burnham et al., 2022).

At the global scale, the Svalbox Digital Model Database (DMDb) (Senger et al., 2021b, a; Betlem et al., 2023b) represents the most comparable initiative in terms of scope. Hosted in Svalbard, the Svalbox DMDb currently comprises several hundred DOMs distributed across a wide range of stratigraphic intervals and geological settings, covering an area extent of several tens of square kilometers. In contrast, although the FATDOM dataset encompasses a more restricted geographic footprint, it provides a dense and systematic coverage of key outcrops within its study area. In terms of spatial resolution, both databases rely on high-resolution photogrammetric workflows, typically achieving centimeter- to sub-centimeter-scale ground sampling distances, allowing detailed structural and sedimentological analyses (e.g., fracture networks, bedding geometries, facies architecture). While the Svalbox DMDb exceeds FATDOM in areal coverage, both databases share similar objectives in terms of providing high-resolution, outcrop-scale digital representations suitable for quantitative geological analysis. Importantly, like the FATDOM dataset, the Svalbox DMDb is openly accessible and compliant with FAIR data principles (Betlem et al., 2023b), which constitutes a crucial quality criterion by ensuring data findability, accessibility, interoperability, and reusability

https://doi.org/10.5194/essd-2026-194
Preprint. Discussion started: 4 May 2026

for the broader geoscientific community. Perhaps equally important, it facilitates re-processing at a later date when more advanced processing algorithms may be able to extract further insights beyond what is possible today.

5.3 Usability of the dataset

In addition to enabling 3D modeling and analysis of LANFs inherited from the pre-Alpine Jurassic rifting phase, the FATDOM datasets also provide an opportunity to characterize and study Alpine structures related to the collisional phase. By generating 3D maps of thrust faults from different deformation phases, we can analyze their intersections and structural relationships. Finally, the FATDOM data can also be used for other purposes, such as the monitoring of glacial melt and mapping of Alpine structures.

5.3.1 3D geometry of Low-Angle Normal Faults

Our DOMs capture the 3D geometry of LANFs preserved in the Err and Bernina units. Model 11, that documents the Piz Jenatsch and Piz Laviner area, is particularly informative because it allows direct observations of both the Err and Jenatsch LANFs and associated extensional allochthonous blocks (Figure 5). Model 11 is a mixed model that combines previously published data from 2022 (Betlem et al., 2023a) and original data acquired the following summer in 2023. This new acquisition enabled us to expand the area covered by increasing the number of photos from 1 082 to 3 045 and the model area from 1.96 km² to 4.08 km². All data were reprocessed following the protocol described above with 15 control points, whereas the georeferencing of the first model was based on GNSS data (total error of 0.25 m). In this area, the Err LANF is consistently located at the top of the Late Paleozoic Albula Granite and can be mapped across the valley.

Visualization and structural interpretation using Virtual Reality Geological Studio (VRGS) (Hodgetts et al., 2015) enable a detailed characterization of the Err LANF surface, which displays a gentle westward dip of approximately 6° (Figures 5B and 5C). Three main lithological assemblages are observed in the hanging wall of the Err LANF: Late Paleozoic K-feldspar–rich granites, polymetamorphic basement rocks, or directly pre-rift Permian and/or Triassic sedimentary units. At Piz Jenatsch, a second LANF (i.e., Jenatsch LANF) is identified, although its cross-cutting relationship with the Err LANF to the west remains debated (Manatschal and Nievergelt, 1997; Epin and Manatschal, 2018). Therefore, the spatial distribution and mapping of LANFs, together with the nature of their footwall and hanging wall are key elements for understanding the architecture and evolution of such extensional structures in this area.

Thanks to the DOMs, the internal structures of allochthonous blocks composed of pre-rift sediments and basement rocks can also be visualized and investigated. Observations and structural interpretation by VRGS allow the identification of lithological units and geometric analyses including measurement of bedding and fractures of these blocks on the virtual outcrop. At Piz Laviner, measurements of pre-rift bedding planes yield SE dips around 30° showing a cut off relationship with the Err LANF (Figure 5D).

https://doi.org/10.5194/essd-2026-194
Preprint. Discussion started: 4 May 2026

Our DOMs provide a framework for future investigations on 1) the interaction and evolution in time and space of LANFs such as the interactions between the Err and Jenatsch structures, 2) the related deformation of the footwall and hanging wall, 3) the formation of extensional allochthons. As shown with model 11, the FATDOM dataset enables a complementary approach by integrating multi-scale observations derived from 3D models with more classical field data, thereby facilitating further investigation of these processes.

https://doi.org/10.5194/essd-2026-194
Preprint. Discussion started: 4 May 2026

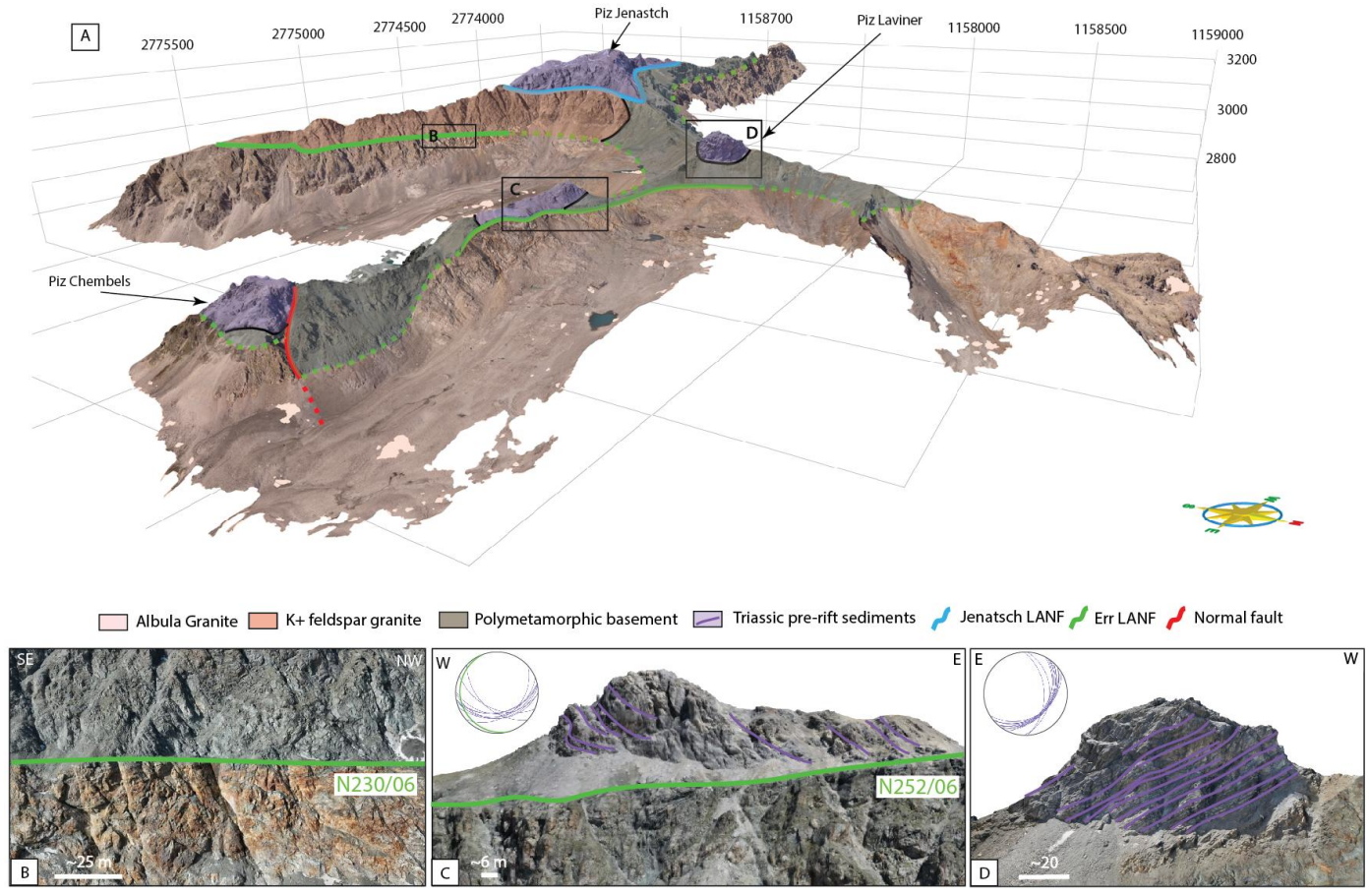

455 **Figure 5: The LANFs system in the Laviner and Jenatsch area imaged by the DOM (model 11). A. Large scale interpretation of the model 11 using VRGS. B. Zoom in the Err LANF surface and the damage zone below Piz Jenatsch. C. Extensional allochthonous block on the Err LANF. D. The extensional allochthonous block of Piz Laviner and orientations of structural elements. The stereographic projection in C and D are presented in lower hemisphere Schmidt projection.**

https://doi.org/10.5194/essd-2026-194
Preprint. Discussion started: 4 May 2026

Open Access Earth System Science Data Discussions

5.3.2 Geological implications of DOMs and comparison with seismic data

Given their regional and seismic-scale extent, the DOMs can be treated as correctly scaled analogues to subsurface settings elsewhere. Specifically, their interpretation allows us to bridge the seismic scale (km) with the outcrop scale (m). The resolution is higher than seismic data, although similar geological objects are observed with comparable size such as extensional allochthons and LANFs. Therefore, the DOMs of this fossil analogue of rifted margin preserved onshore can provide critical new information on extensional structures leading to the formation of hyper-extended rift basin. Such observations can be compared with present day rifted margin imaged offshore by 3D seismic surveys. An example of such comparison is shown in Figure 6. It illustrates the Jurassic rift-related extensional structures of Piz Jenatsch along the fossil Adriatic margin (model 11) shown in Figure 5. Similar structures are imaged along the present-day southern passive margin of the South China Sea where hyper-extended basins controlled by normal faults formed and were active at low angle (Legeay et al., 2024).

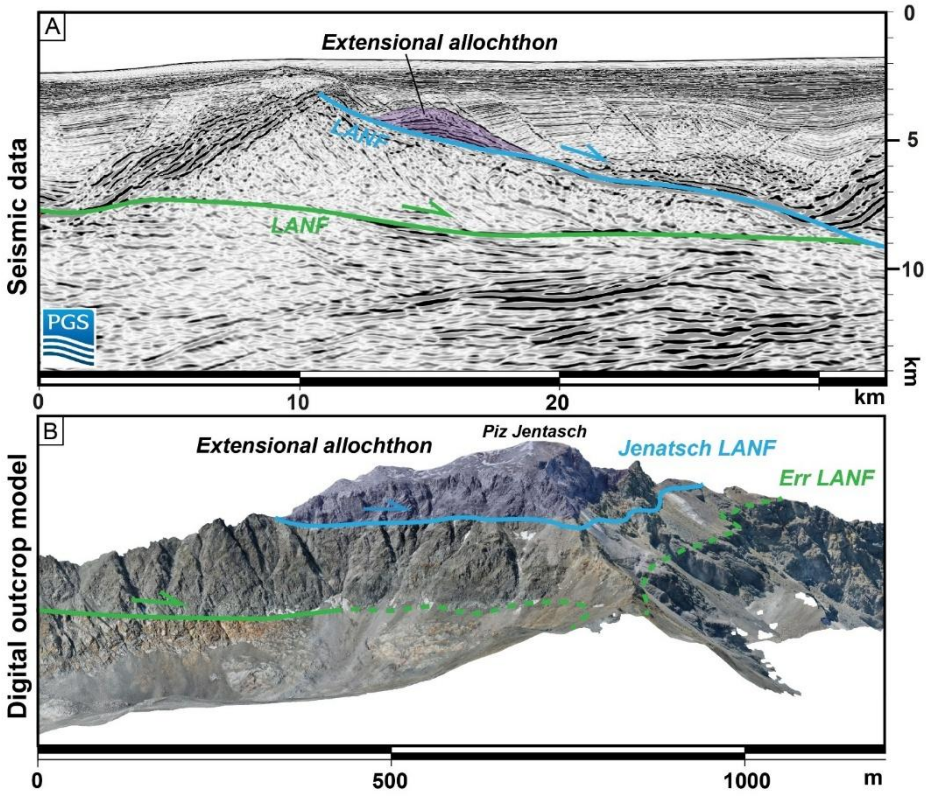

Figure 6: A. Seismic cross-section across a hyper-extended basin in the Southern margin of the South China Sea, modified from Legeay et al., (2024). B. Zoom on the model 11 (Figure 5), where Jurassic rift related extensional structures are observed.

https://doi.org/10.5194/essd-2026-194
Preprint. Discussion started: 4 May 2026

This comparison highlights the development of LANFs during rifting leading to the formation of allochthonous blocks of pre-rift sediments. In both cases, the LANFs are interpreted to develop sequentially and transport pre-rift sedimentary blocks that lie on the active fault surface. LANFs are increasingly imaged in seismic reflection data triggering new questions regarding their development and implication in controlling the formation of hyper-extended basins (Sapin et al., 2021) as discussed by Lymer et al. (2019) for the Galicia margin or Lymer et al. (2023) for West of Ireland. As a result, an iterative approach between observations in present-day hyper-extended basins and fossil analogues will be one of the keys for a better understanding of LANF systems and associated sedimentary basins.

5.3.3 Use in geomorphology: monitoring deglaciation

Models that include glaciers, such as the Vadret Traunter Ovas glacier in model 2 of 2023 (Piz Surgonda and Corn margun) and the Vadret d'Err glacier in the model 7 (Jenatsch south 1) of 2024, can serve as valuable tools to evaluate glacier evolution (Figure 7). By comparing the 2022 Swisstopo reference datasets with the FATDOM DEMs and orthomosaics, we can assess glacier changes over this period. It is also possible to incorporate older datasets from Swisstopo's national coverage, as DEMs are available upon request since 2008 (Swisstopo, 2022a), and orthomosaics since 1998 (Swisstopo, 2022b), with the added benefit that the FATDOM dataset resolution is up to an order of magnitude higher.

https://doi.org/10.5194/essd-2026-194
Preprint. Discussion started: 4 May 2026

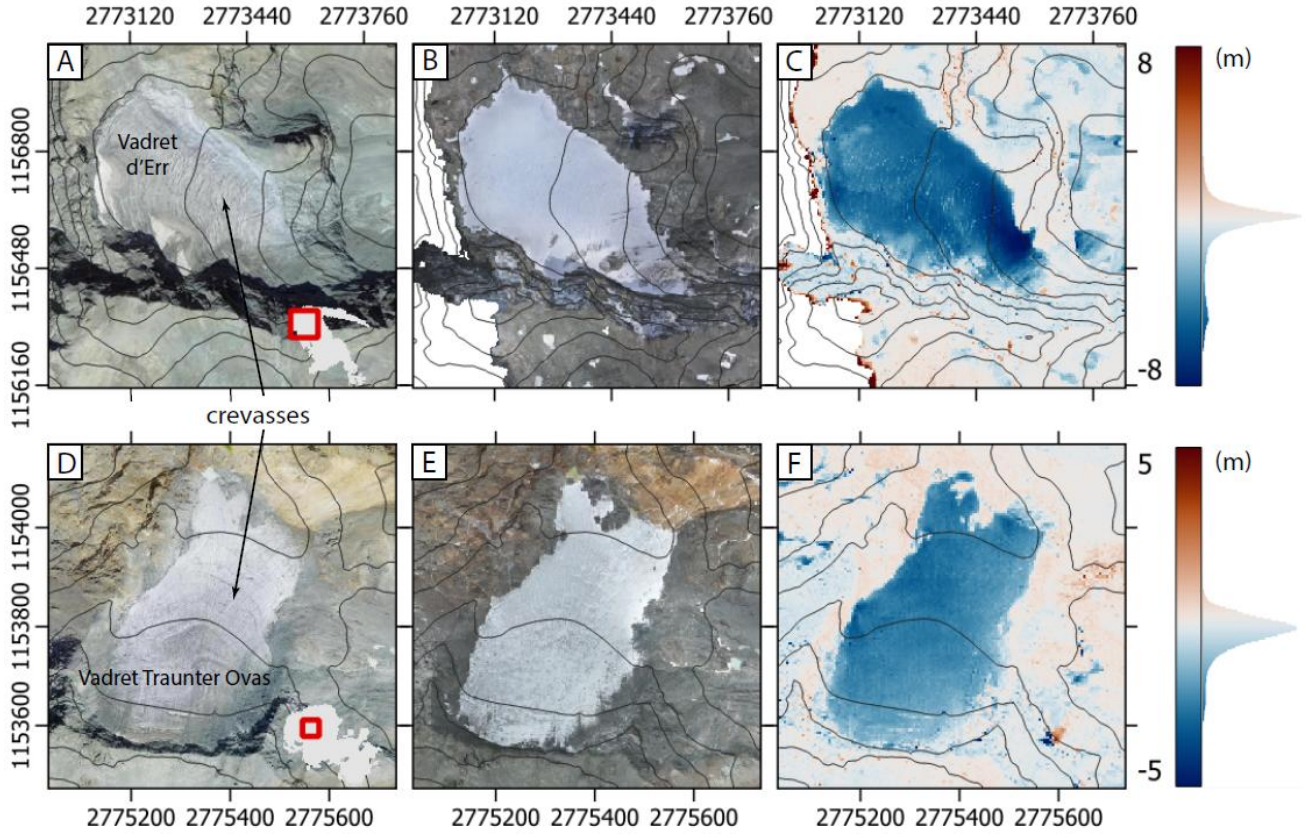

Figure 7: A. Swisstopo orthomosaic of the Vadret d'Err glacier (2022), including its location in the model 7. B. Zoom-in of model 7 showing the orthomosaic covering the Vadret d'Err glacier (2024). C. DEM comparison map of the Vadret d'Err glacier between the model 7 DEM and the Swisstopo DEM, and the histogram deviation showing the repartition of the differences. D. Swisstopo orthomosaic of the Vadret Traunter Ovas glacier (2022), including its location in model 2. E. Zoom-in of model 2 showing the orthomosaic covering of the Vadret Traunter Ovas glacier (2023). F. DEM comparison map of the Vadret Traunter Ovas glacier between the model 2 DEM and the Swisstopo DEM, and the histogram deviation showing the repartition of the differences.

Examination of the DEM comparison map in the Vadret d'Err glacier area (Figure 7C) shows significant variations between the Swisstopo DEM and model 7 DEM. These negative deviations around -4.5 m correspond to the glacier's location. After delineating the surface of the Vadret d'Err glacier from the orthomosaics (Figure 5A et 5B), we estimated a volume loss of approximately -918 918.46 m^3 across the entire surface of the glacier between 2022 and 2024. Similarly, we observed a significant variation on the DEM comparison map (Figure 7F) with negative deviation around -2m where the Vardet Traunter Ovas glacier is located. The comparison of the data (Figure 7D et 7E) allows us to outline the glacier and calculate a volume loss of -301 971.59 m^3 for this glacier between 2022 and 2023.

https://doi.org/10.5194/essd-2026-194
Preprint. Discussion started: 4 May 2026

Thus, the photogrammetric approach remains relevant and can be applied to future acquisitions, using the FATDOM dataset as a reference. As such, it provides a dated baseline model to evaluate glacier changes in the coming years within the context of climate change. The comparison also allows us to comment on surface characteristics, and to observe crevasses (Figure 7A et 7D), accumulation zones and ablation zones, as well as the presence of debris, all of which may have a major influence on glacier dynamics and melting.

6 Data availability

The full FATDOM dataset, including input images, metashape projects and processing reports; DEMs, DOMs, orthomosaics and tiled models, can be freely downloaded from the Zenodo data repository under FAIR conditions : https://doi.org/10.5281/zenodo.18940068 (Morzelle et al., 2026). Visualization and interpretation are possible through opensource, freeware (e.g. Agisoft's Viewer, QGIS (Dawson et al., 2026)) and commercial software like LIME (Buckley et al., 2019) and VRGS (Hodgetts et al., 2015; Buckley et al., 2022).

The full dataset consists of 12 individual data packages, each includes the following files and zipped archives for a given model:

- data.zip: archive containing input UAV imagery, including disabled photos, and input differential GNSS data.
- export.zip: archive containing DOM, DEM, orthomosaic and tiled model in CH1903+/LV95 (EPSG:2056) projection system. For model 11 we added the measurements presented in Figure 5 and extracted from VRGS (folder measurements).
- metashape.zip: archive containing the Agisoft Metashape project featuring sparse and dense point clouds, mesh-including textures, tiled model, DOM, DEM and orthomosaics
- processing reports: in pdf and in html
- Readme
- Overview image

Individual models can be accessed at the following DOIs (Table 5) : model 1 https://doi.org/10.5281/zenodo.18999037 (Morzelle et al., 2026d); model 2 https://doi.org/10.5281/zenodo.18313841 (Morzelle et al., 2026e); model 3 https://doi.org/10.5281/zenodo.18313845 (Morzelle et al., 2026f); model 4 https://doi.org/10.5281/zenodo.18313853 (Morzelle et al., 2026g); model 5 https://doi.org/10.5281/zenodo.18313864 (Morzelle et al., 2026h); model 6 https://doi.org/10.5281/zenodo.18313874 (Morzelle et al., 2026i); model 7 https://doi.org/10.5281/zenodo.18313880 (Morzelle et al., 2026j); model 8 https://doi.org/10.5281/zenodo.18313886 (Morzelle et al., 2026k); model 9 https://doi.org/10.5281/zenodo.18313891 (Morzelle et al., 2026l); model 10 https://doi.org/10.5281/zenodo.18313898

https://doi.org/10.5194/essd-2026-194
Preprint. Discussion started: 4 May 2026

(Morzelle et al., 2026m); model 11 https://doi.org/10.5281/zenodo.18313900 (Morzelle et al., 2026b); model 12 https://doi.org/10.5281/zenodo.18313906 (Morzelle et al., 2026c).

535 **Table 5: DOIs of the models stored on Zenodo and size of the files.**

Digital outcrop model	Orthomosaic	DOI	Size of the data (GB)
Piz Bardella		https://doi.org/10.5281/zenodo.18999037	23.34
Piz Surgonda and Corn Margun		https://doi.org/10.5281/zenodo.18313841	47.61
Piz d'Err and Piz Calderas		https://doi.org/10.5281/zenodo.18313845	58.17
Piz d'Alp Val and Piz Bial		https://doi.org/10.5281/zenodo.18313853	15.36
Fuorcla d'Agnel south		https://doi.org/10.5281/zenodo.18313864	20.47
Fuorcla d'Agnel north		https://doi.org/10.5281/zenodo.18313874	19.76
Piz Jenatsch south 1		https://doi.org/10.5281/zenodo.18313880	19.76
Piz Jenatsch south 2		https://doi.org/10.5281/zenodo.18313886	4.46
Corn Alv		https://doi.org/10.5281/zenodo.18313891	11.78

https://doi.org/10.5194/essd-2026-194
Preprint. Discussion started: 4 May 2026

Piz Neir	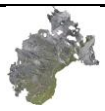	https://doi.org/10.5281/zenodo.18313898	33.03
Laviner and Jenatsch area		https://doi.org/10.5281/zenodo.18313900	146.31
Val da Fain		https://doi.org/10.5281/zenodo.18313906	88.93

7 Code availability

The processing pages (supplementary materiel) have been uploaded to the Zenodo data repository under this DOI: https://doi.org/10.5281/zenodo.18417132 (Morzelle et al., 2026a).

8 Conclusion

This paper presents the new acquisition of photogrammetric data, processing methodology, and quality control of 12 DOMs capturing the remnants of former distal rifted margin located in Swiss Alps. These DOMs represent a first step towards the digitalization of key geological structures, such as LANFs that have been described over decades of detailed geological studies. The following conclusions are drawn:

- The FATDOM dataset covers 43 km² of the Err and Bernina units, belonging to the Lower Austroalpine nappes, and is composed of 12 DOMs, georeferenced with metric positioning errors constrained using Swisstopo datasets as a reference.
- All data are openly available to the geoscience community under FAIR (Findable, Accessible, Interoperable, and Reusable) conditions.
- Accurate georeferencing of the 12 models was achieved through a combined use of PPK data, GCPs and CPs. Comparison with the Swisstopo reference dataset only shows local discrepancies, mainly related to differences in acquisition procedures, particularly in steep cliffs and areas affected by seasonal or landscape variability (e.g., glaciers and scree slopes).
- With a centimeter- to decimeter-scale resolution, the dataset provides detailed observations on some previously inaccessible outcrops showing former rift-related structures such as LANFs. This dataset offers new perspectives for addressing first order geological problems such as the 3D evolution of LANFs accommodating the final thinning of

https://doi.org/10.5194/essd-2026-194
Preprint. Discussion started: 4 May 2026

the continental lithosphere. It paves the way for dedicated follow-up work on the characterization of LANFs and for the testing of new rifting models involving allochthonous block formation.

- This dataset enables 3D geological interpretations and quantitative study of outcrop-scale structures using both open and proprietary softwares. It can also be used to compare and complement observations of LANFs from present-day seismic data across multiple rifted margins.
- Finally, it plays a key role in preserving and safeguarding critical geological heritage in a setting heavily affected by ongoing climate change.

In closing, we hope that this collection of data will be useful both to the structural geology community, by improving the understanding of extensional processes, oceanic opening, and subsequent Alpine collision responsible for the present-day mountain belt, and to the geomorphology community interested in landscape evolution driven by climate-related processes such as glaciation and erosion.

Author contributions

Leïla Morzelle: Writing – original draft, Writing – review & editing, Visualization, Validation, Methodology, Investigation, Formal analysis, Data curation, Conceptualization. **Peter Betlem**: Writing – review & editing, Visualization, Validation, Supervision, Visualization, Software, Methodology, Investigation, Formal analysis, Data curation, Conceptualization. **Geoffroy Mohn**: Writing – review & editing, Visualization, Supervision, Project administration, Investigation, Funding acquisition, Formal analysis, Conceptualization. **Julie Tugend**: Writing – review & editing, Visualization, Supervision, Investigation, Formal analysis, Conceptualization.

Competing interests

The authors declare that they have no conflict of interest.

Acknowledgements

The Laundenbacher foundation is acknowledged for accommodation during the extensive field campaigns. Totalenergies and TGS are thanked for permission to publish the seismic data. Lucie Poudevigne is warmly thanked for her help during field data acquisition of model 10. Chat GPT was used to improve the English of the manuscript.

https://doi.org/10.5194/essd-2026-194
Preprint. Discussion started: 4 May 2026

Open Access Earth System Science Data Discussions

Financial support

This study is part of G. Mohn's NFETRA project funded by CY Initiative, a program supported by the French National Research Agency (ANR) under the French government grant: “Investissements d'avenir” #France 2030 (ANR-16-IDEX-0008). We also acknowledge basic funding given to NGI from the Research Council of Norway (RCN).

References

Betlem, P., Mohn, G., Tugend, J., and Manatschal, G.: High-resolution digital outcrop models of fossil-rifted margins: 3D imaging of extensional detachment systems, First Break, 41, 31–40, https://doi.org/10.3997/1365-2397.fb2023032, 2023a.

Betlem, P., Rodés, N., Birchall, T., Dahlin, A., Smyrak-Sikora, A., and Senger, K.: Svalbox Digital Model Database: A geoscientific window into the High Arctic, Geosphere, 19, 1640–1666, https://doi.org/10.1130/GES02606.1, 2023b.

Betlem, P., Birchall, T., Lord, G., Oldfield, S., Nakken, L., Ogata, K., and Senger, K.: High-resolution digital outcrop model of the faults, fractures, and stratigraphy of the Agardhfjellet Formation cap rock shales at Konusdalen West, central Spitsbergen, Earth Syst. Sci. Data, 16, 985–1006, https://doi.org/10.5194/essd-16-985-2024, 2024.

Betlem, P., Rodes, N., Cohen, S. M., and Vander Kloet, M. A.: Jupyter Book as an open online teaching environment in the geosciences: lessons learned from Geo-SfM and Geo-UAV, Geosci. Commun., 8, 51–65, https://doi.org/10.5194/gc-8-51-2025, 2025.

Bistacchi, A., Balsamo, F., Storti, F., Mozafari, M., Swennen, R., Solum, J., Tueckmantel, C., and Taberner, C.: Photogrammetric digital outcrop reconstruction, visualization with textured surfaces, and three-dimensional structural analysis and modeling: Innovative methodologies applied to fault-related dolomitization (Vajont Limestone, Southern Alps, Italy), Geosphere, 11, 2031–2048, https://doi.org/10.1130/GES01005.1, 2015.

Buck, W. R.: flexural rotation of normal faults, Tectonics, 7, 959–973, https://doi.org/10.1029/TC007i005p00959, 1988.

Buckley, S. J., Ringdal, K., Naumann, N., Dolva, B., Kurz, T. H., Howell, J. A., and Dewez, T. J. B.: LIME: Software for 3-D visualization, interpretation, and communication of virtual geoscience models, Geosphere, 15, 222–235, https://doi.org/10.1130/GES02002.1, 2019.

Buckley, S. J., Howell, J. A., Naumann, N., Lewis, C., Chmielewska, M., Ringdal, K., Vanbiervliet, J., Tong, B., Mulelid-Tynes, O. S., Foster, D., Maxwell, G., and Pugsley, J.: V3Geo: a cloud-based repository for virtual 3D models in geoscience, Geosci. Commun., 5, 67–82, https://doi.org/10.5194/gc-5-67-2022, 2022.

Burnham, B., Bond, C., Flaig, P., Van Der Kolk, D., and Hodgetts, D.: Outcrop conservation: Promoting accessibility, inclusivity, and reproducibility through digital preservation, Sediment. Rec., 20, https://doi.org/10.2110/sedred.2022.1.2, 2022.

Burnham, B., Bond, C., Flaig, P., Van Der Kolk, D., and Hodgetts, D.: Outcrop conservation: Promoting accessibility, inclusivity, and reproducibility through digital preservation, Sediment. Rec., 20, https://doi.org/10.2110/sedred.2022.1.2, 2024.

https://doi.org/10.5194/essd-2026-194
Preprint. Discussion started: 4 May 2026

Cawood, A. and Bond, C.: eRock: An Open-Access Repository of Virtual Outcrops for Geoscience Education, GSA Today, 29, 36–37, https://doi.org/10.1130/GSATG373GW.1, 2019.

Collettini, C.: The mechanical paradox of low-angle normal faults: Current understanding and open questions, Tectonophysics, 510, 253–268, https://doi.org/10.1016/j.tecto.2011.07.015, 2011.

Dawson, N., Fischer, J., Kuhn, M., Pasotti, A., mhugent, Rouzaud, D., Bruy, A., Sutton, T., Dobias, M., Pellerin, M., Rouault, E., Olaya, V., Blottiere, P., Macho, W., Blazek, R., Bartoletti, L., Sherman, G., Sant-anna, H., Cabieces, J., Woodrow, N., signedav, rldhont, Natsis, S., Shaffer, L., Belgacem, N., Felder, J., Santilli, S., Larosa, S., Mani, S., and Jurgiel, B.: qgis/QGIS: 3.44.8, , https://doi.org/10.5281/zenodo.18889145, 2026.

Dering, G. M., Micklethwaite, S., Thiele, S. T., Vollgger, S. A., and Cruden, A. R.: Review of drones, photogrammetry and emerging sensor technology for the study of dykes: Best practises and future potential, J. Volcanol. Geotherm. Res., 373, 148–166, https://doi.org/10.1016/j.jvolgeores.2019.01.018, 2019.

Epin, M. -E. and Manatschal, G.: Three-Dimensional Architecture, Structural Evolution, and Role of Inheritance Controlling Detachment Faulting at a Hyperextended Distal Margin: The Example of the Err Detachment System (SE Switzerland), Tectonics, 37, 4494–4514, https://doi.org/10.1029/2018TC005125, 2018.

Ferreiro Mählmann, R.: Das Diagenese-Metamorphose-Muster von Vitrinitreflexion und Illit-"Kristallinität" in Mittelbünden und im Oberhalbstein, Teil 1 : Bezüge zur Stockwerktektonik = The pattern of diagenesis and metamorphism by vitrinite reflectance and illite-"crystallinity" in Mittelbünden and in the Oberhalbstein, Part 1 : the Relationship to stockwerk tectonics, https://doi.org/10.5169/SEALS-57145, 1995.

Froitzheim, N. and Eberli, G. P.: Extensional detachment faulting in the evolution of a Tethys passive continental margin, Eastern Alps, Switzerland, 1990.

Froitzheim, N., Schmid, S. M., and Conti, P.: Repeated change from crustal shortening to orogen-parallel extension in the Austroalpine units of Graubünden, https://doi.org/10.5169/SEALS-167471, 1994.

Gindraux, S., Boesch, R., and Farinotti, D.: Accuracy Assessment of Digital Surface Models from Unmanned Aerial Vehicles' Imagery on Glaciers, Remote Sens., 9, 186, https://doi.org/10.3390/rs9020186, 2017.

Hodgetts, D., Seers, T., Head, W., and Burnham, B. S.: High Performance Visualisation of Multiscale Geological Outcrop Data in Single Software Environment, 77th EAGE Conference and Exhibition 2015, 1–5, https://doi.org/10.3997/2214-4609.201412862, 2015.

Howell, J. and Burnham, B.: The Virtual Geoscience Revolution: From William Smith to Virtual Outcrop, https://doi.org/10.31223/X5MS66, 29 July 2021.

James, M. R., Chandler, J. H., Eltner, A., Fraser, C., Miller, P. E., Mills, J. P., Noble, T., Robson, S., and Lane, S. N.: Guidelines on the use of structure-from-motion photogrammetry in geomorphic research, Earth Surf. Process. Landf., 44, 2081–2084, https://doi.org/10.1002/esp.4637, 2019.

Lecomte, E., Le Pourhiet, L., and Lacombe, O.: Mechanical basis for slip along low-angle normal faults, Geophys. Res. Lett., 39, 2011GL050756, https://doi.org/10.1029/2011GL050756, 2012.

https://doi.org/10.5194/essd-2026-194
Preprint. Discussion started: 4 May 2026

Legeay, E., Mohn, G., Ringenbach, J. C., Vetel, W., and Sapin, F.: 3D Structure of Low-Angle Normal Faults and Tectono-Sedimentary Processes of Nascent Continental Core-Complexes in the SE South China Sea, Tectonics, 43, e2023TC008218, https://doi.org/10.1029/2023TC008218, 2024.

Lymer, G., Cresswell, D. J. F., Reston, T. J., Bull, J. M., Sawyer, D. S., Morgan, J. K., Stevenson, C., Causer, A., Minshull, T. A., and Shillington, D. J.: 3D development of detachment faulting during continental breakup, Earth Planet. Sci. Lett., 515, 90–99, https://doi.org/10.1016/j.epsl.2019.03.018, 2019.

Lymer, G., Childs, C., and Walsh, J.: Punctuated propagation of a corrugated extensional detachment offshore Ireland, Basin Res., 35, 1037–1052, https://doi.org/10.1111/bre.12745, 2023.

Manatschal, G.: New models for evolution of magma-poor rifted margins based on a review of data and concepts from West Iberia and the Alps, Int. J. Earth Sci., 93, https://doi.org/10.1007/s00531-004-0394-7, 2004.

Manatschal, G. and Nievergelt, P.: A continent-ocean transition recorded in the Err and Platta nappes (Eastern Switzerland), Eclogae Geol. Helvetiae, 90(1), 3–27, 1997.

Manatschal, G., Chenin, P., Ghienne, J., Ribes, C., and Masini, E.: The syn-rift tectono-stratigraphic record of rifted margins (Part I): Insights from the Alpine Tethys, Basin Res., 34, 457–488, https://doi.org/10.1111/bre.12627, 2022.

Manna, L., Perozzo, M., Menegoni, N., Tamburelli, S., Crispini, L., Federico, L., Seno, S., and Maino, M.: Anatomy of a km-scale fault zone controlling the Oligo-Miocene bending of the Ligurian Alps (NW Italy): integration of field and 3D high-resolution digital outcrop model data, Swiss J. Geosci., 116, 15, https://doi.org/10.1186/s00015-023-00444-1, 2023.

Masini, E., Manatschal, G., Mohn, G., and Unternehr, P.: Anatomy and tectono-sedimentary evolution of a rift-related detachment system: The example of the Err detachment (central Alps, SE Switzerland), Geol. Soc. Am. Bull., 124, 1535–1551, https://doi.org/10.1130/B30557.1, 2012.

McCarthy, A., Tugend, J., and Mohn, G.: Formation of the Alpine Orogen by Amagmatic Convergence and Assembly of Previously Rifted Lithosphere, Elements, 17, 29–34, https://doi.org/10.2138/gselements.17.1.29, 2021.

Melosh, H. J.: Mechanical basis for low-angle normal faulting in the Basin and Range province, Nature, 343, 331–335, https://doi.org/10.1038/343331a0, 1990.

Menegoni, N., Giordan, D., and Perotti, C.: Reliability and Uncertainties of the Analysis of an Unstable Rock Slope Performed on RPAS Digital Outcrop Models: The Case of the Gallivaggio Landslide (Western Alps, Italy), Remote Sens., 12, 1635, https://doi.org/10.3390/rs12101635, 2020.

Mohn, G., Manatschal, G., Müntener, O., Beltrando, M., and Masini, E.: Unravelling the interaction between tectonic and sedimentary processes during lithospheric thinning in the Alpine Tethys margins, Int. J. Earth Sci., 99, 75–101, https://doi.org/10.1007/s00531-010-0566-6, 2010.

Mohn, G., Manatschal, G., Masini, E., and Müntener, O.: Rift-related inheritance in orogens: a case study from the Austroalpine nappes in Central Alps (SE-Switzerland and N-Italy), Int. J. Earth Sci., 100, 937–961, https://doi.org/10.1007/s00531-010-0630-2, 2011.

https://doi.org/10.5194/essd-2026-194
Preprint. Discussion started: 4 May 2026

Mohn, G., Manatschal, G., Beltrando, M., Masini, E., and Kusznir, N.: Necking of continental crust in magma-poor rifted margins: Evidence from the fossil Alpine Tethys margins, Tectonics, 31, 2011TC002961, https://doi.org/10.1029/2011TC002961, 2012.

Morzelle, L, Betlem, P., Mohn, G., and Tugend, J.: FATDOM-DB, https://doi.org/10.5281/zenodo.18940068, 2026.

Morzelle, L, Betlem, P., Mohn, G., and Tugend J.: FATDOM-DB supplementary materiel, https://doi.org//10.5281/zenodo.18417132, 2026a.

Morzelle, L., Betlem, P., Mohn, G., and Tugend, J.: FATDOM-DB_2022-2023-0011, https://doi.org/10.5281/zenodo.18313900, 2026b.

Morzelle, L., Betlem, P., Mohn, G., and Tugend, J.: FATDOM-DB_2022-2023-0012, https://doi.org/10.5281/zenodo.18313906, 2026c.

Morzelle, L., Betlem, P., Mohn, G., and Tugend, J.: FATDOM-DB_2023-0001, https://doi.org/10.5281/zenodo.18999037, 2026d.

Morzelle, L., Betlem, P., Mohn,G., and Tugend, J.: FATDOM-DB_2023-0002, https://doi.org/10.5281/zenodo.18313841, 2026e.

Morzelle, L., Betlem, P., Mohn,G., and Tugend, J.: FATDOM-DB_2023-0003, https://doi.org/10.5281/zenodo.18313845, 2026f.

Morzelle, L., Betlem, P., Mohn,G., and Tugend, J.: FATDOM-DB_2023-0004, https://doi.org/10.5281/zenodo.18313853, 2026g.

Morzelle, L., Betlem, P., Mohn,G., and Tugend, J.: FATDOM-DB_2024-0005, https://doi.org/10.5281/zenodo.18313864, 2026h.

Morzelle, L., Betlem, P., Mohn, G., and Tugend, J.: FATDOM-DB_2024-0006, https://doi.org/10.5281/zenodo.18313874, 2026i.

Morzelle, L., Betlem, P., Mohn, G., and Tugend, J.: FATDOM-DB_2024-0007, https://doi.org/10.5281/zenodo.18313880, 2026j.

Morzelle, L., Betlem, P., Mohn, G., and Tugend, J.: FATDOM-DB_2024-0008, https://doi.org/10.5281/zenodo.18313886, 2026k.

Morzelle, L., Betlem, P., Mohn, G., and Tugend, J.: FATDOM-DB_2024-0009, https://doi.org/10.5281/zenodo.18313891, 2026l.

Morzelle, L., Betlem, P., Mohn, G., and Tugend, J.: FATDOM-DB_2025-0010, https://doi.org//10.5281/zenodo.18313898, 2026m.

https://doi.org/10.5194/essd-2026-194
Preprint. Discussion started: 4 May 2026

Ribes, C., Manatschal, G., Ghienne, J.-F., Karner, G. D., Johnson, C. A., Figueredo, P. H., Incerpi, N., and Epin, M.-E.: The syn-rift stratigraphic record across a fossil hyper-extended rifted margin: the example of the northwestern Adriatic margin exposed in the Central Alps, Int. J. Earth Sci., 108, 2071–2095, https://doi.org/10.1007/s00531-019-01750-6, 2019.

Sapin, F., Ringenbach, J.-C., and Clerc, C.: Rifted margins classification and forcing parameters, Sci. Rep., 11, 8199, https://doi.org/10.1038/s41598-021-87648-3, 2021.

Senger, K., Betlem, P., Grundvåg, S.-A., Horota, R. K., Buckley, S. J., Smyrak-Sikora, A., Jochmann, M. M., Birchall, T., Janocha, J., Ogata, K., Kuckero, L., Johannessen, R. M., Lecomte, I., Cohen, S. M., and Olaussen, S.: Teaching with digital geology in the high Arctic: opportunities and challenges, Geosci. Commun., 4, 399–420, https://doi.org/10.5194/gc-4-399-2021, 2021a.

Senger, K., Betlem, P., Birchall, T., Buckley, S. J., Coakley, B., Eide, C. H., Flaig, P. P., Forien, M., Galland, O., Gonzaga, L., Jensen, M., Kurz, T., Lecomte, I., Mair, K., Malm, R. H., Mulrooney, M., Naumann, N., Nordmo, I., Nolde, N., Ogata, K., Rabbel, O., Schaaf, N. W., and Smyrak-Sikora, A.: Using digital outcrops to make the high Arctic more accessible through the Svalbox database, J. Geosci. Educ., 69, 123–137, https://doi.org/10.1080/10899995.2020.1813865, 2021b.

Swisstopo: SwissALTI3D - High-resolution DEM of Switzerland, Swisstopo, 2022a.

Swisstopo: SWISSIMAGE - Orthophotos mosaic of Switzerland, Swisstopo, 2022b.

Thiele, S. T., Micklethwaite, S., Bourke, P., Verrall, M., and Kovesi, P.: Insights into the mechanics of en-échelon sigmoidal vein formation using ultra-high resolution photogrammetry and computed tomography, J. Struct. Geol., 77, 27–44, https://doi.org/10.1016/j.jsg.2015.05.006, 2015.

Wernicke, B.: Low-angle normal faults in the Basin and Range Province: nappe tectonics in an extending orogen, Nature, 291, 645–648, https://doi.org/10.1038/291645a0, 1981.

Wilkinson, M. D., Dumontier, M., Aalbersberg, Ij. J., Appleton, G., Axton, M., Baak, A., Blomberg, N., Boiten, J.-W., Da Silva Santos, L. B., Bourne, P. E., Bouwman, J., Brookes, A. J., Clark, T., Crosas, M., Dillo, I., Dumon, O., Edmunds, S., Evelo, C. T., Finkers, R., Gonzalez-Beltran, A., Gray, A. J. G., Groth, P., Goble, C., Grethe, J. S., Heringa, J., 'T Hoen, P. A. C., Hooft, R., Kuhn, T., Kok, R., Kok, J., Lusher, S. J., Martone, M. E., Mons, A., Packer, A. L., Persson, B., Rocca-Serra, P., Roos, M., Van Schaik, R., Sansone, S.-A., Schultes, E., Sengstag, T., Slater, T., Strawn, G., Swertz, M. A., Thompson, M., Van Der Lei, J., Van Mulligen, E., Velterop, J., Waagmeester, A., Wittenburg, P., Wolstencroft, K., Zhao, J., and Mons, B.: The FAIR Guiding Principles for scientific data management and stewardship, Sci. Data, 3, 160018, https://doi.org/10.1038/sdata.2016.18, 2016.

https://doi.org/10.5194/essd-2026-194
Preprint. Discussion started: 4 May 2026

Appendix A

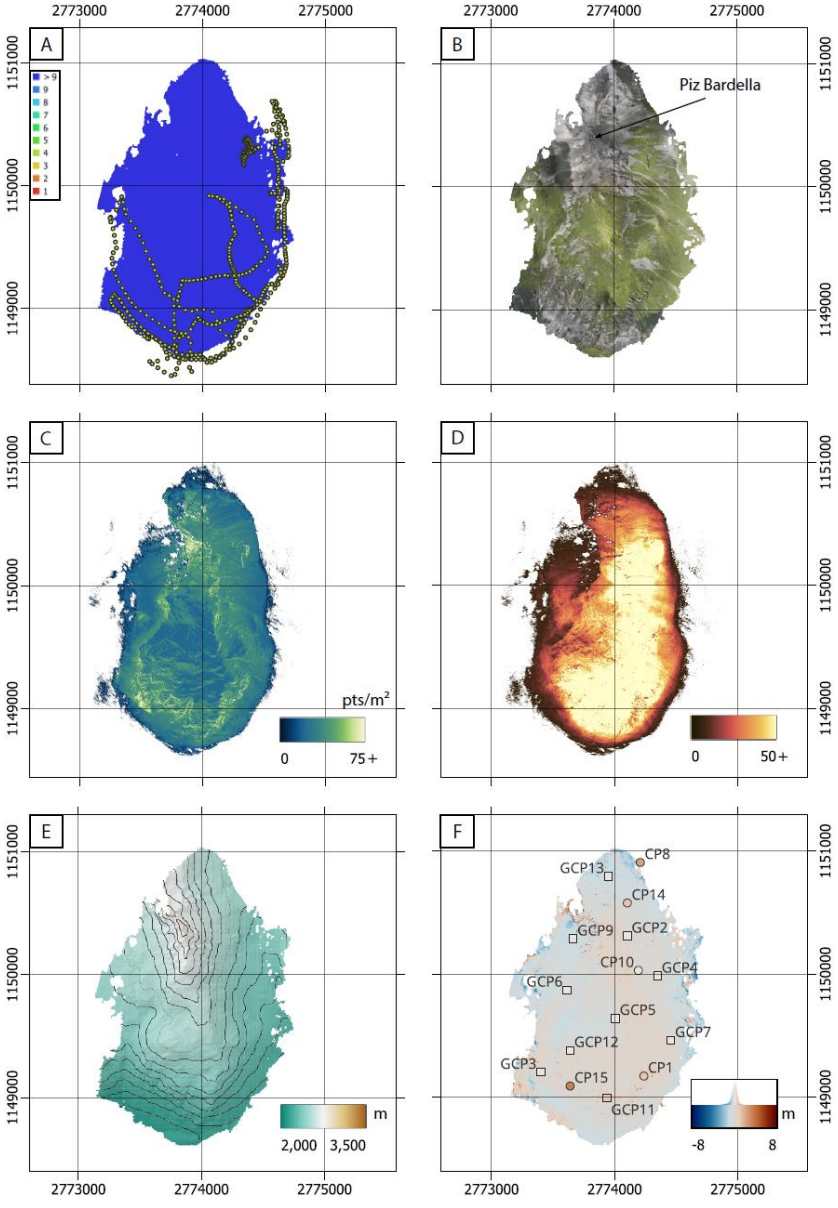

Figure A1: Detailed data overview of Piz Bardella DOM (model 1). A. Camera locations (yellow dots) and image overlap indicate good coverage with a majority covered by at least 9 images. B. The Orthomosaic has a spatial resolution of 10.7 cm/pix. C. The density of the dense cloud is ranging from 0 to ≥75 points/m², lower in the periphery and highest in the geological interest outcrops. D. The confidence, average of all points over a square meter, of the dense cloud ranges from 0 to ≥50. E. The DEM presents elevation values ranging from 2 040 m to 2 850 m, has a spatial resolution of 21.5 cm/pixels. F. The DEM comparison map based on the reference SwissALTI3D DEM and the histogram of deviation distribution shows that across most of the model, the differences are close to 0, and between -2 and 2.5 m.

https://doi.org/10.5194/essd-2026-194
Preprint. Discussion started: 4 May 2026

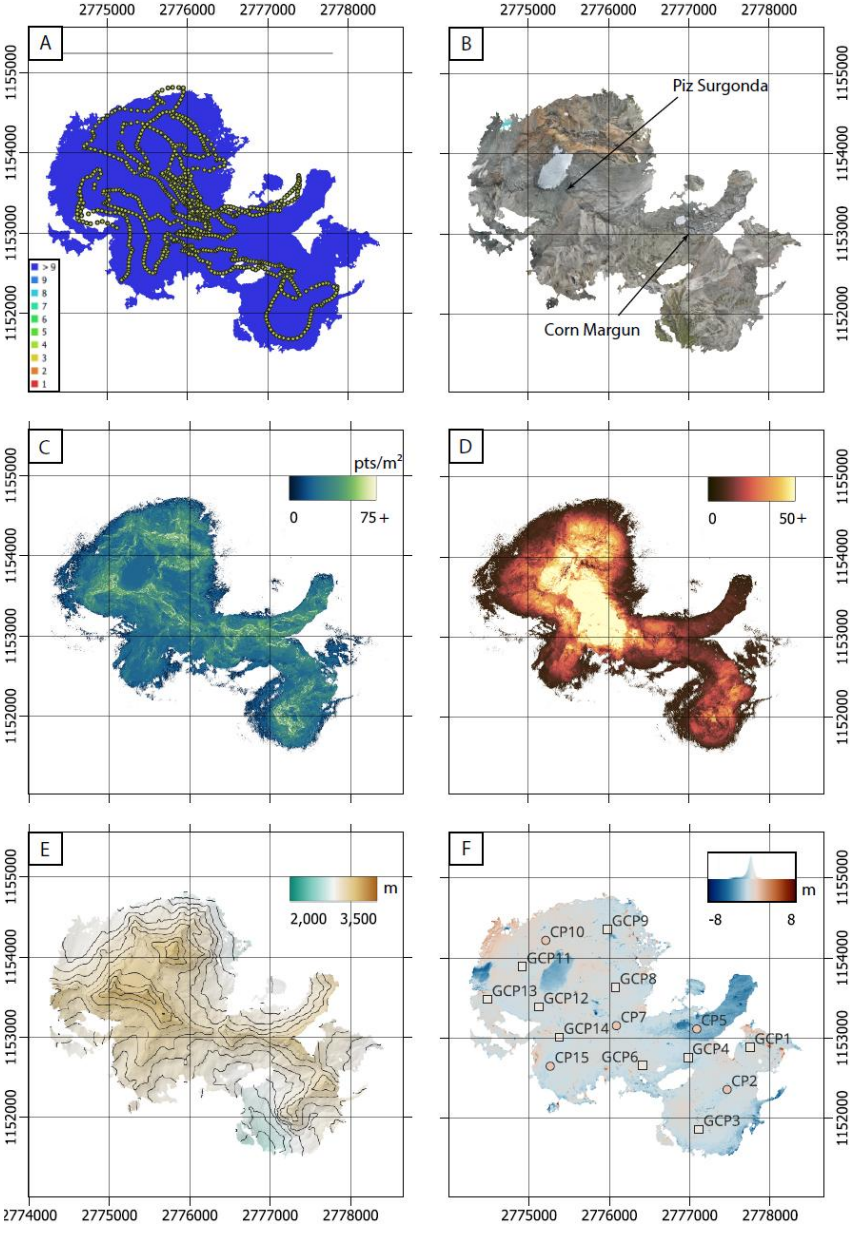

Figure A2: Detailed data overview of Piz Surgonda and Corn Margun DOM (model 2). A. Camera locations (yellow dots) and image overlap indicate good coverage with a majority covered by at least 9 images. B. The Orthomosaic has a spatial resolution of 10.9 cm/pix. C. The density of the dense is ranging from 0 to ≥75 points/m², lower in the periphery and highest in the geological interest outcrops. D. The confidence, average of all points over a square meter, of the dense cloud ranges from 0 to ≥50. E. The DEM presents elevation values ranging from 2 050 m to 3 200 m, has a spatial resolution of 21.7 cm/pixels. F. The DEM comparison map based on the reference SwissALTI3D DEM and the histogram of deviation distribution shows that across most of the model, the differences are close to 0, and between -4 and 2 m.

https://doi.org/10.5194/essd-2026-194
Preprint. Discussion started: 4 May 2026

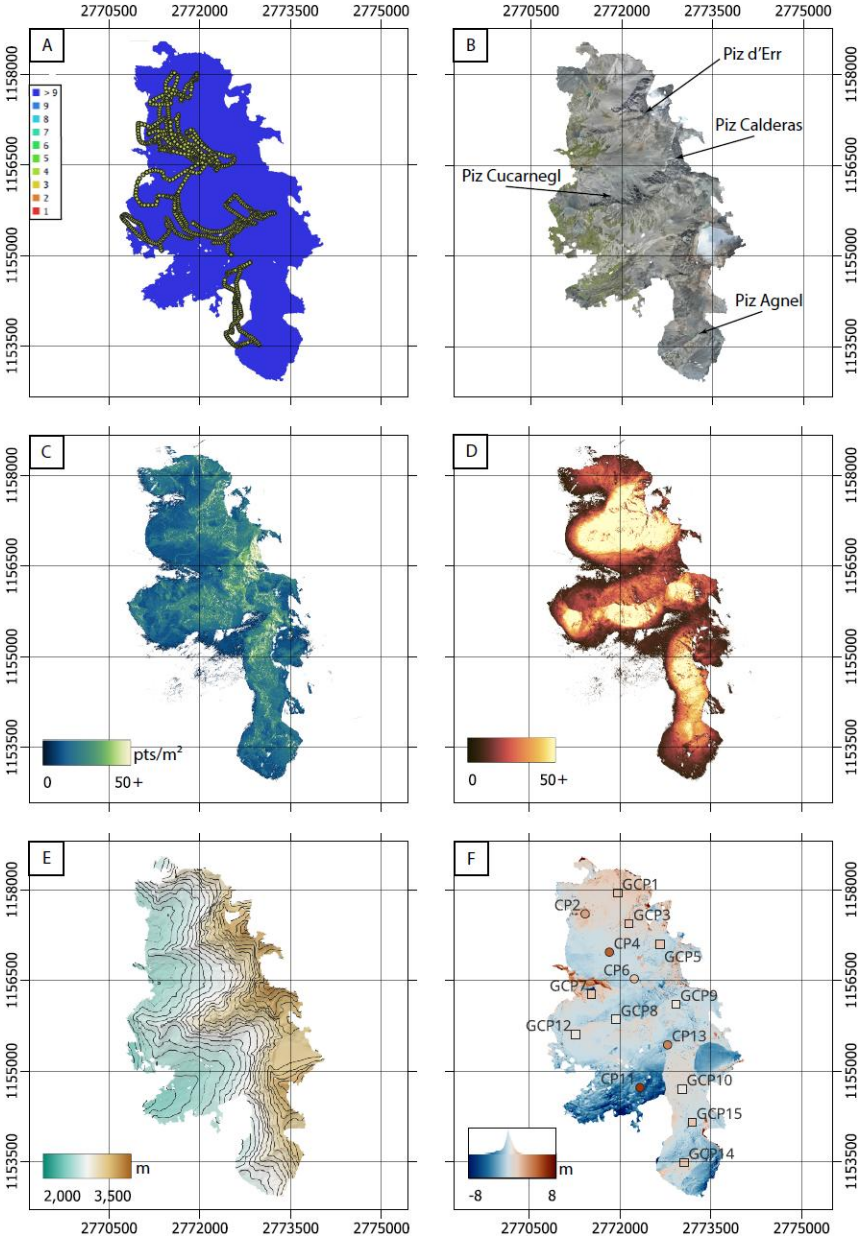

Figure A3: Detailed data overview of Piz d'Err and Piz Calderas DOM (model 3). A. Camera locations (yellow dots) and image overlap indicate good coverage with a majority covered by at least 9 images. B. The Orthomosaic has a spatial resolution of 15.4 cm/pix. C. The density of the dense cloud is ranging from 1 to ≥50 points/m², lower in the periphery and highest in the geological interest outcrops. D. The confidence, average of all points over a square meter, of the dense cloud ranges from 0 to ≥50. E. The DEM presents elevation values ranging from 2 200 m to 3 400 m, has a spatial resolution of 30.9 cm/pixels. F. The DEM comparison map based on the reference SwissALTI3D DEM and the histogram of deviation distribution shows that across most of the model, the differences are close to 0, and between -6.5 and 5 m.

https://doi.org/10.5194/essd-2026-194
Preprint. Discussion started: 4 May 2026

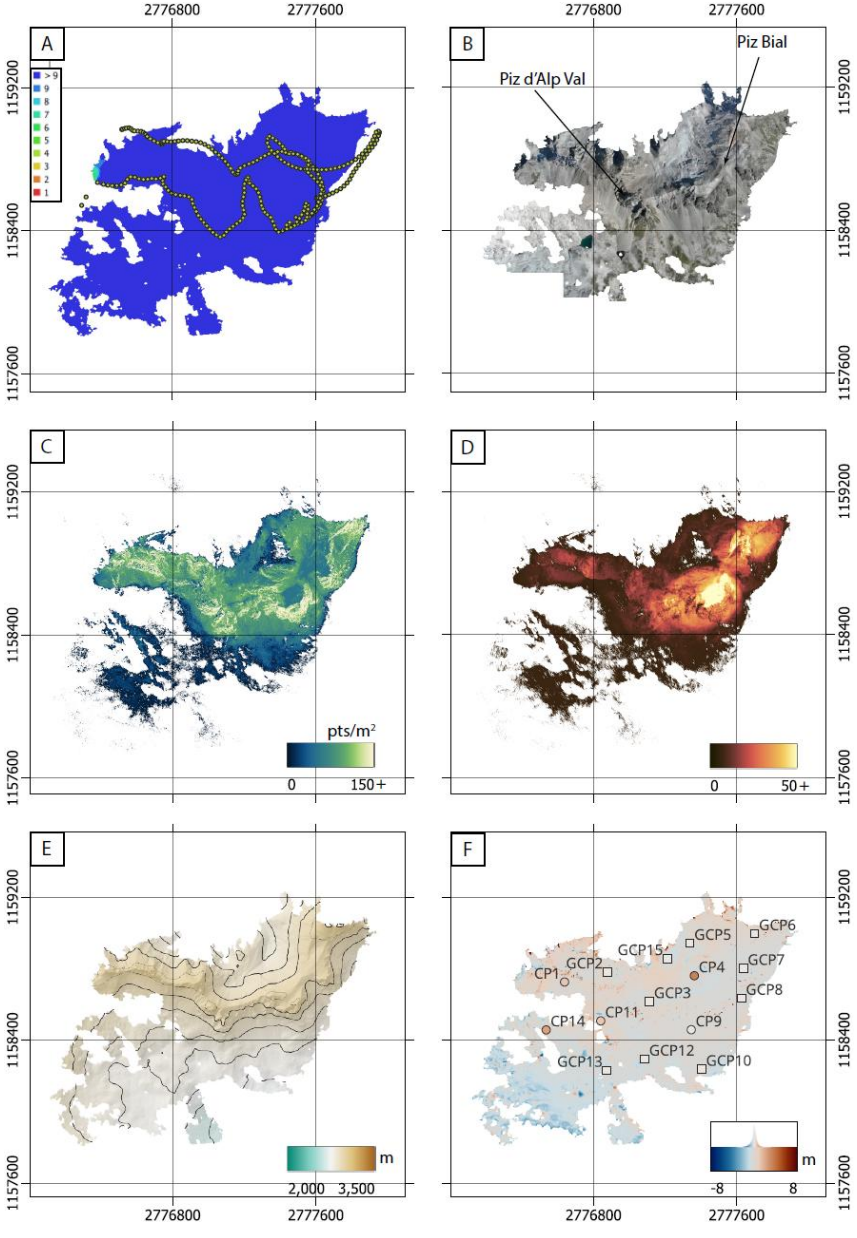

Figure A4: Detailed data overview of Piz d'Alp Val and Piz Bial DOM (model 4). A. Camera locations (yellow dots) and image overlap indicate good coverage with a majority covered by at least 9 images. B. The Orthomosaic has a spatial resolution of 6.85 cm/pix. C. The density of the dense cloud is ranging from 0 to ≥150 points/m², lower in the periphery and of highest in the geological interest outcrops. D. The confidence, average of all points over a square meter, of the dense cloud ranges from 0 to ≥50. E. The DEM presents elevation values ranging from 2 630 m to 3 070 m, has a spatial resolution of 13.7 cm/pixels. F. The DEM comparison map based on the reference SwissALTI3D DEM and the histogram of deviation distribution shows that across most of the model, the differences are close to 0, and between -2.5 and 2 m.

https://doi.org/10.5194/essd-2026-194
Preprint. Discussion started: 4 May 2026

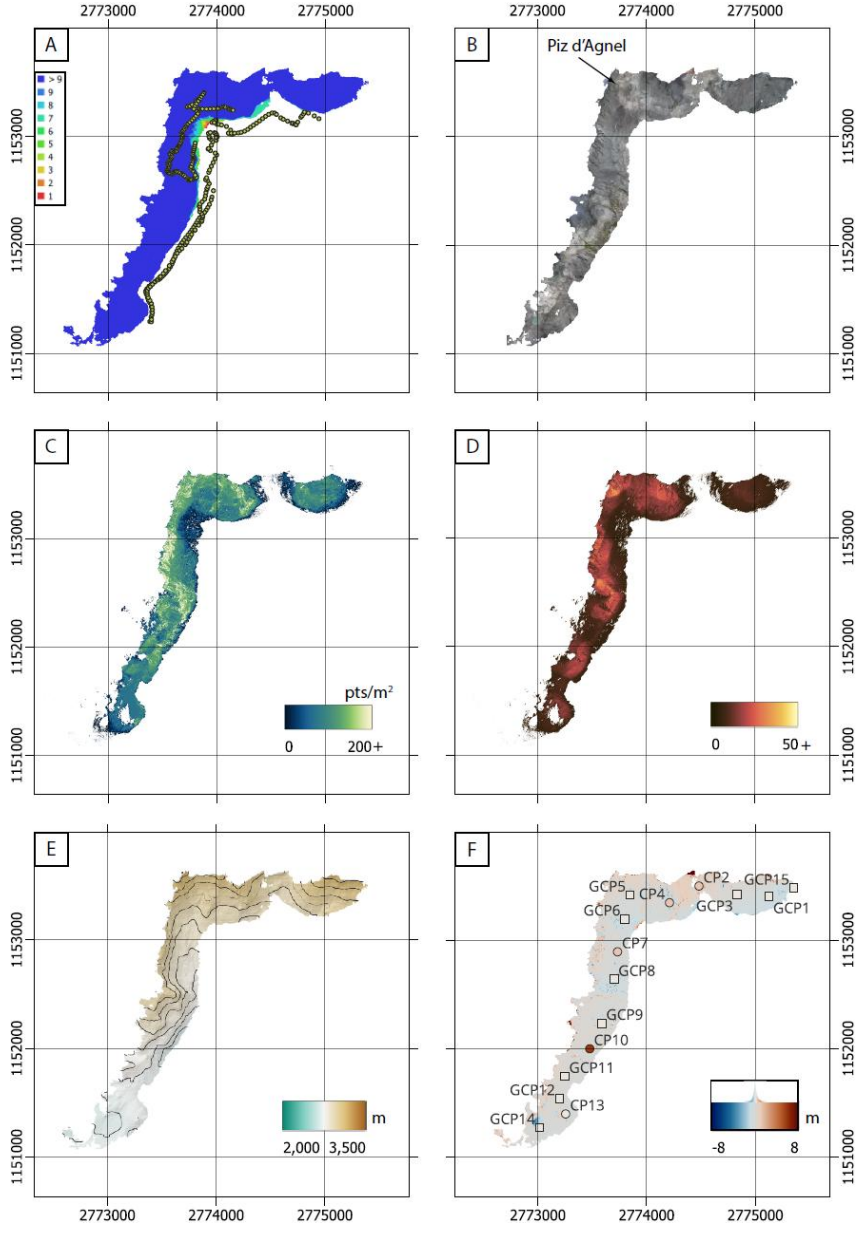

Figure A5: Detailed data overview of Fuorcla d'Agnel south DOM (model 5). A. Camera locations (yellow dots) and image overlap indicate good coverage with a majority covered by at least 9 images. B. The Orthomosaic has a spatial resolution of 5.98 cm/pix. C. The density of the dense cloud is ranging from 0 to ≥400 points/m², lower in the periphery and highest in the geological interest outcrops. D. The confidence, average of all points over a square meter, of the dense cloud ranges from 1 to ≥50. E. The DEM presents elevation values ranging from 2 640 m to 3 210 m, has a spatial resolution of 12 cm/pixels. F. The DEM comparison map based on the reference SwissALTI3D DEM and the histogram of deviation distribution shows that across most of the model, the differences are close to 0, and between -1.75 and 1.75 m.

https://doi.org/10.5194/essd-2026-194
Preprint. Discussion started: 4 May 2026

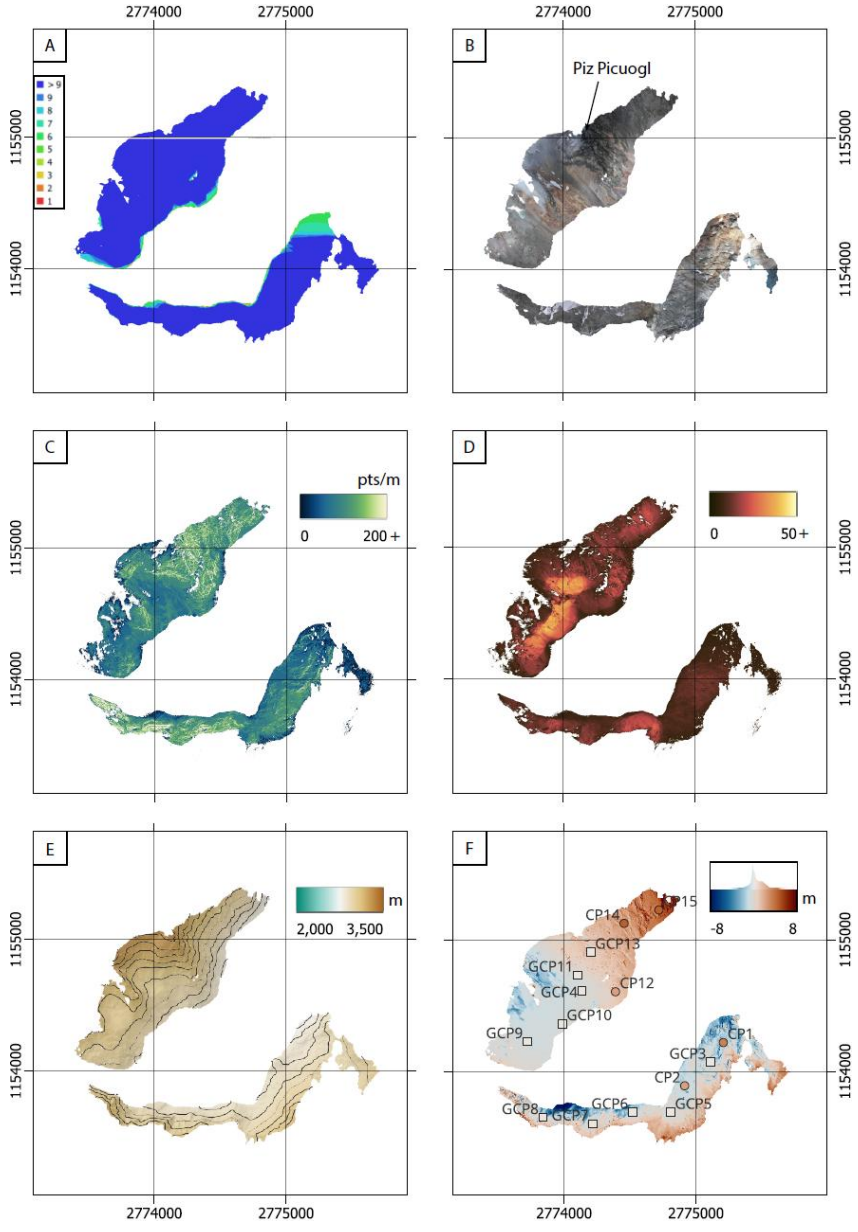

Figure A6: Detailed data overview of Fuorcla d'Agnel north DOM (model 6). A. Camera locations (yellow dots) and image overlap indicate good coverage with a majority covered by at least 9 images. B. The Orthomosaic has a spatial resolution of 6.44 cm/pix. C. The density of the dense cloud is ranging from 0 to ≥200 points/m², lower in the periphery and highest in the geological interest outcrops. D. The confidence, average of all points over a square meter, of the dense cloud ranges from 0 to ≥50. E. The DEM presents elevation values ranging from 2 760 m to 3 340 m, has a spatial resolution of 12.9 cm/pixels. F. The DEM comparison map based on the reference SwissALTI3D DEM and the histogram of deviation distribution shows that across most of the model, the differences are close to 0, and between -5 and 7 m.

https://doi.org/10.5194/essd-2026-194
Preprint. Discussion started: 4 May 2026

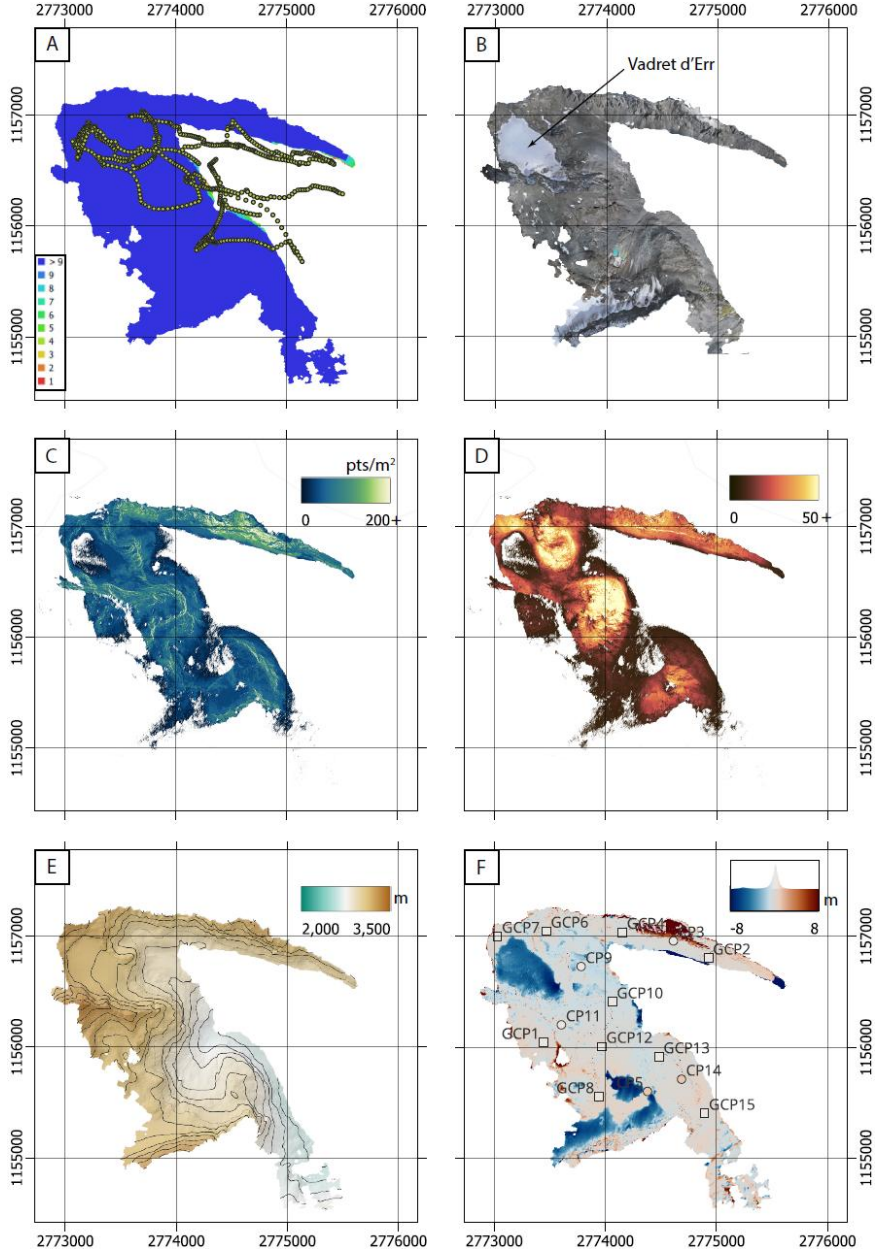

795 **Figure A7: Detailed data overview of Piz Jenatsch south 1 DOM (model 7). A. Camera locations (yellow dots) and image overlap indicate good coverage with a majority covered by at least 9 images. B. The Orthomosaic has a spatial resolution of 8.67 cm/pix. C. The density of the dense cloud is ranging from 1 to ≥200 points/m², lower in the periphery and highest in the geological interest outcrops. D. The confidence, average of all points over a square meter, of the dense cloud ranges from 0 to ≥50. E. The DEM presents elevation values ranging from 2 580 m to 3 400 m, has a spatial resolution of 17.3 cm/pixels. F. The DEM comparison map based on**
800 **the reference SwissALTI3D DEM and the histogram of deviation distribution shows that across most of the model, the differences are close to 0, and between -7 and 4 m.**

https://doi.org/10.5194/essd-2026-194
Preprint. Discussion started: 4 May 2026

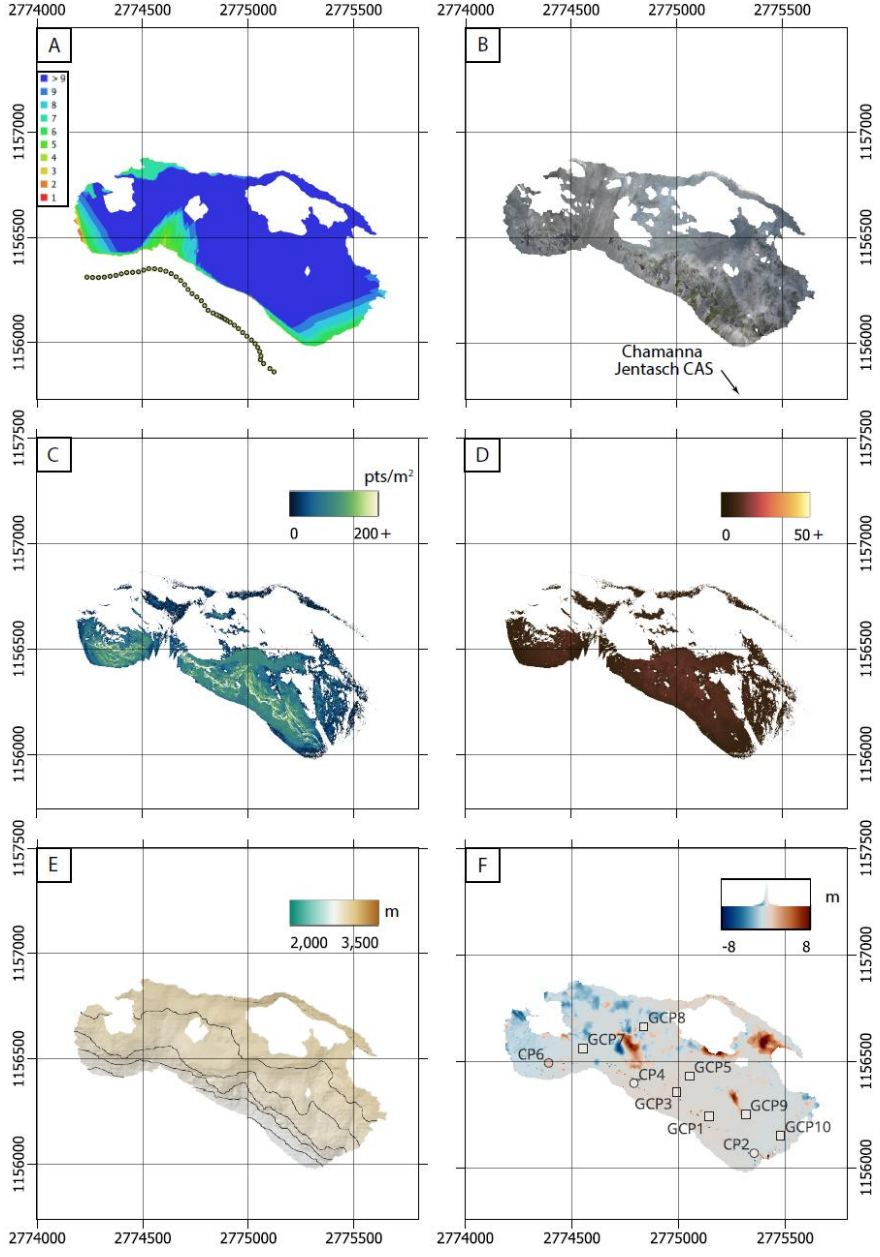

Figure A8: Detailed data overview of Piz Jenatsch south 2 DOM (model 8). A. Camera locations (yellow dots) and image overlap indicate good coverage with a majority covered by at least 9 images. B. The Orthomosaic has a spatial resolution of 6.5 cm/pix. C. The density of the dense cloud is ranging from 0 to ≥200 points/m², lower in the periphery and highest in the geological interest outcrops. D. The confidence, average of all points over a square meter, of the dense cloud ranges from 0 to ≥50. E. The DEM presents elevation values ranging from 2 710 m to 3 040 m, has a spatial resolution of 13 cm/pixels. F. The DEM comparison map based on the reference SwissALTI3D DEM and the histogram of deviation distribution shows that across most of the model, the differences are close to 0, and between -3 and 2.5 m.

https://doi.org/10.5194/essd-2026-194
Preprint. Discussion started: 4 May 2026

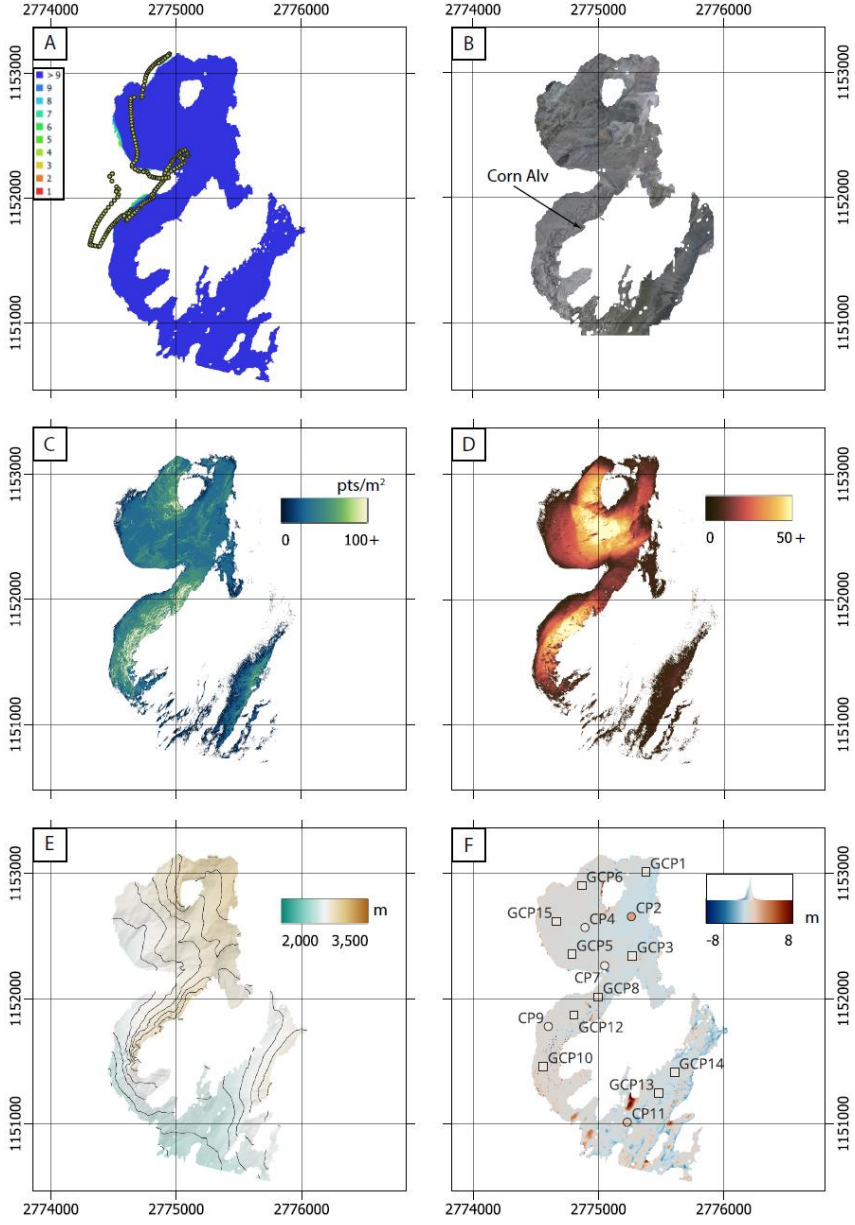

Figure A9: Detailed data overview of Corn Alv DOM (model 9). A. Camera locations (yellow dots) and image overlap indicate good coverage with a majority covered by at least 9 images. B. The Orthomosaic has a spatial resolution of 9 cm/pix. C. The density of the dense cloud is ranging from 0 to ≥100 points/m², lower in the periphery and highest in the geological interest outcrops. D. The confidence, average of all points over a square meter, of the dense cloud ranges from 0 to ≥50. E. The DEM presents elevation values ranging from 2 510 m to 3 010 m, has a spatial resolution of 18 cm/pixels. F. The DEM comparison map based on the reference SwissALTI3D DEM and the histogram of deviation distribution shows that across most of the model, the differences are close to 0, and between -2.6 and 2.3 m.

https://doi.org/10.5194/essd-2026-194
Preprint. Discussion started: 4 May 2026

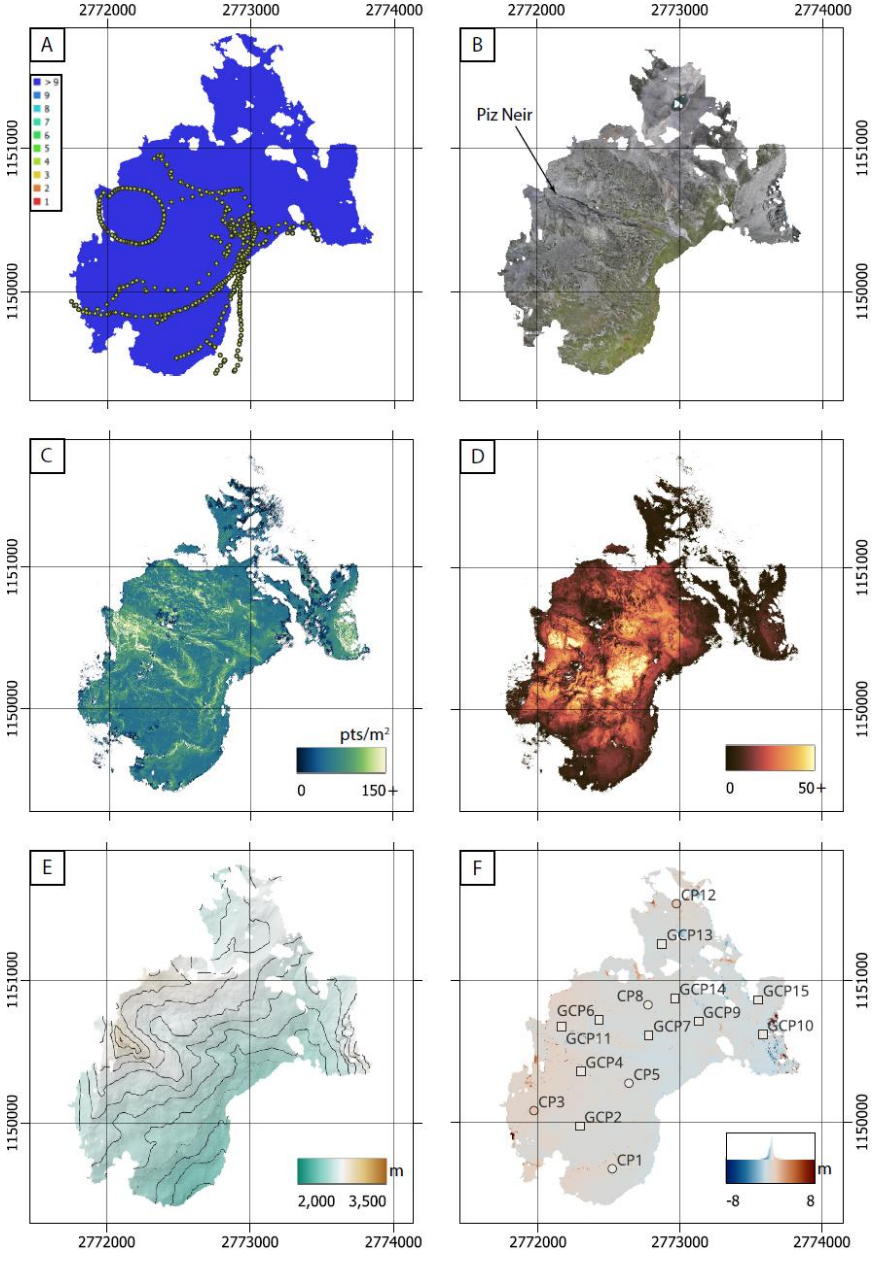

Figure A10: Detailed data overview of Piz Neir DOM (model 10). A. Camera locations (yellow dots) and image overlap indicate good coverage with a majority covered by at least 9 images. B. The Orthomosaic has a spatial resolution of 7.13 cm/pix. C. The density of the dense cloud is ranging from 0 to ≥150 points/m², lower in the periphery and highest in the geological interest outcrops. D. The confidence, average of all points over a square meter, of the dense cloud ranges from 0 to ≥50. E. The DEM presents elevation values ranging from 2 330 m to 2 910 m, has a spatial resolution of 14.3 cm/pixels. F. The DEM comparison map based on the reference SwissALTI3D DEM and the histogram of deviation distribution shows that across most of the model, the differences are close to 0, and between -1.5 and 1.5 m.

https://doi.org/10.5194/essd-2026-194
Preprint. Discussion started: 4 May 2026

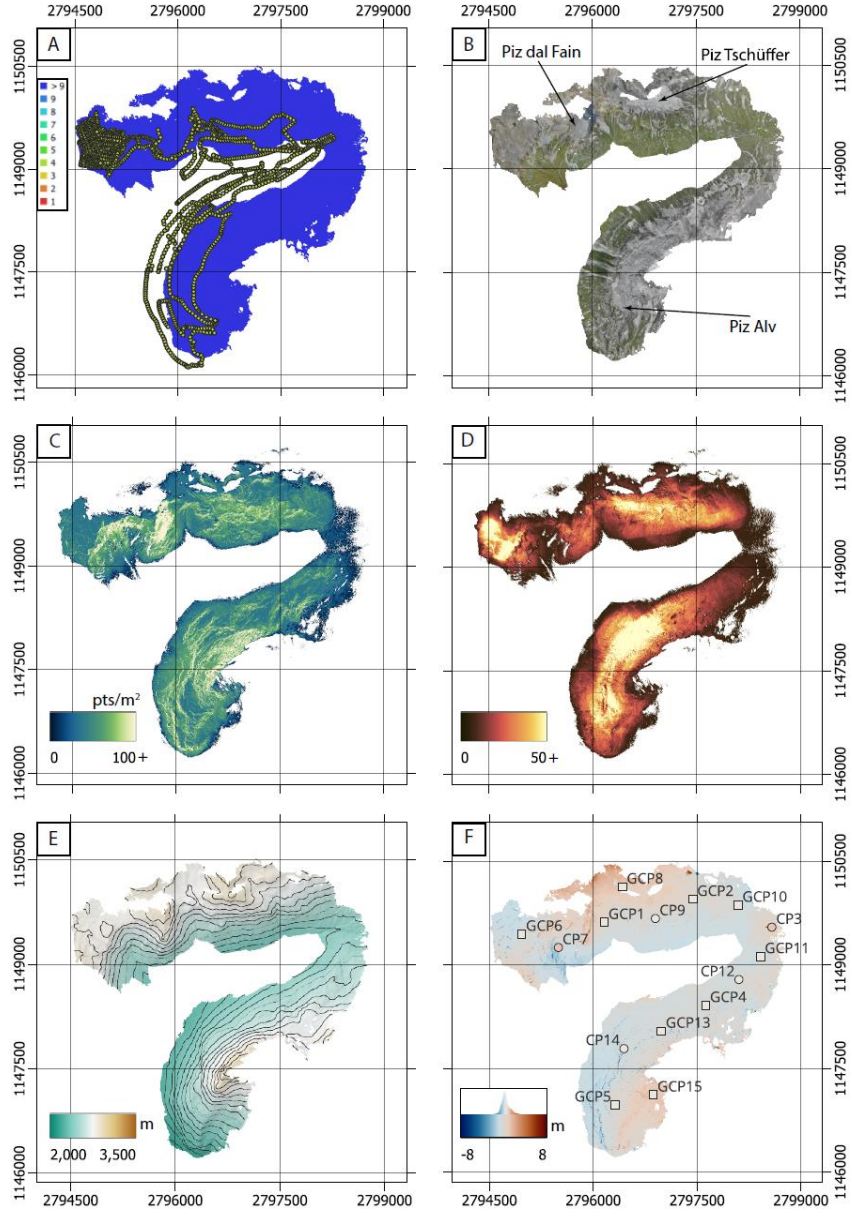

Figure A11: Detailed data overview of Val da Fain DOM (model 12). A. Camera locations (yellow dots) and image overlap indicate good coverage with a majority covered by at least 9 images. B. The Orthomosaic has a spatial resolution of 8.36 cm/pix. C. The density of the dense cloud is ranging from 0 to ≥100 points/m², lower in the periphery and highest in the geological interest outcrops. D. The confidence, average of all points over a square meter, of the dense cloud ranges from 0 to ≥50. E. The DEM presents elevation values ranging from 2 130 m to 3 030 m, has a spatial resolution of 16.7 cm/pixels. F. The DEM comparison map based on the reference SwissALTI3D DEM and the histogram of deviation distribution shows that across most of the model, the differences are close to 0, and between -2.3 and 2.5.

https://doi.org/10.5194/essd-2026-194
Preprint. Discussion started: 4 May 2026

Open Access Earth System Science Data Discussions

Appendix B

Table B1: Ground control points (GCPs) and check points (CPs) used for high-resolution georeferencing of the Piz Bardella DOM (model 1). Easting and northing given in the EPSG:2056 reference system.

Marker	Type	Images	Northing (y, m)	Easting (x, m)	Altitude (m)	Northing estimation (y, m)	Easting estimation (x, m)	Altitude estimation (m)	Northing variance (y, m)	Easting variance (x, m)	Altitude variance (m)	Error (x,m)	Error (y, m)	Error (z, m)	Error (xyz, m)
2	GCP	87	1150310.033	2774104.678	2593.265869	1150310.264	2774104.746	2593.412789	0.007974	0.007492	0.007836	0.067986	0.231562	0.14692	0.282539
3	GCP	41	1149203.676	2773400.521	2240.135742	1149203.812	2773400.915	2240.058103	0.009433	0.009734	0.010961	0.394286	0.136309	-0.077639	0.424346
4	GCP	64	1149986.342	2774349.219	2389.822754	1149985.764	2774349.141	2389.99092	0.007827	0.007266	0.009079	-0.078096	-0.578553	0.168166	0.607538
5	GCP	79	1149640.983	2774006.757	2559.807129	1149640.837	2774007.06	2560.053796	0.006244	0.0061	0.00655	0.303359	-0.146407	0.246667	0.417501
6	GCP	39	1149870.959	2773612.447	2498.790039	1149870.477	2773612.67	2498.728798	0.007842	0.006623	0.007875	0.223216	-0.481572	-0.061241	0.534311
7	GCP	67	1149460.506	2774456.054	2303.43042	1149460.662	2774456.025	2303.66095	0.008683	0.008726	0.011008	-0.029106	0.156519	0.23053	0.280159
8	GCP	21	1150909.419	2774209.425	2490.540039	1150910.675	2774208.979	2489.856214	0.047872	0.013298	0.020404	-0.446156	1.256467	-0.683825	1.49846
11	GCP	104	1148991.972	2773936.882	2289.794678	1148992.414	2773935.982	2289.64505	0.008892	0.008973	0.009783	-0.900873	0.442702	-0.149628	1.014862
12	GCP	78	1149379.327	2773638.545	2467.116943	1149378.995	2773638.596	2466.921947	0.007078	0.006956	0.007606	0.051237	-0.331727	-0.194997	0.38819
13	GCP	18	1150796.443	2773950.513	2599.767822	1150795.758	2773950.927	2600.142858	0.013053	0.011017	0.011847	0.41412	-0.685276	0.375036	0.884166
Total GCP error												0.386475	0.551281	0.290226	0.733148
1	CP	84	1149171.101	2774238.032	2352.141357	1149170.792	2774238.487	2352.198595	0.008419	0.008663	0.010171	0.455735	-0.308877	0.057238	0.553512
9	CP	38	1150287.39	2773662.433	2611.612061	1150287.239	2773662.394	2611.528512	0.010297	0.008562	0.00949	-0.039629	-0.150777	-0.083548	0.176875
10	CP	142	1150030.967	2774192.77	2485.199951	1150030.816	2774193.105	2485.270119	0.006892	0.006506	0.007465	0.335289	-0.150882	0.070168	0.374309
14	CP	39	1150579.866	2774103.613	2559.119873	1150580.492	2774103.764	2558.412104	0.010124	0.013765	0.010966	0.150714	0.626882	-0.707769	0.95741
15	CP	82	1149089.851	2773638.894	2246.585205	1149089.936	2773636.652	2245.380266	0.008885	0.008792	0.009469	-2.242426	0.084578	-1.204939	2.547058
Total CP error												1.03662	0.32895	0.627374	1.25554

Table B2: Ground control points (GCPs) and check points (CPs) used for high-resolution georeferencing of the Piz Surgonda and Corn Margun DOM (model 2). Easting and northing given in the EPSG:2056 reference system.

Marker	Type	Images	Northing (y, m)	Easting (x, m)	Altitude (m)	Northing estimation (y, m)	Easting estimation (x, m)	Altitude estimation (m)	Northing variance (y, m)	Easting variance (x, m)	Altitude variance (m)	Error (x,m)	Error (y, m)	Error (z, m)	Error (xyz, m)
1	GCP	23	1152887.742	2777753.765	2843.84375	1152887.732	2777753.77	2843.837565	0.000825	0.000826	0.000826	0.004127	-0.009752	-0.006185	0.012263
3	GCP	22	1151863.948	2777115.656	2676.312256	1151863.949	2777115.66	2676.311226	0.000826	0.000826	0.000827	0.003681	0.000777	-0.00103	0.0039
4	GCP	31	1152758.764	2776979.151	2833.01001	1152758.791	2776979.142	2833.030588	0.000816	0.000818	0.000822	-0.009833	0.02637	0.020578	0.034864
6	GCP	10	1152660.876	2776416.101	2812.778564	1152660.857	2776416.094	2812.765242	0.000815	0.000819	0.000824	-0.006803	-0.019089	-0.013323	0.024252
8	GCP	59	1153636.053	2776075.259	2891.7771	1153636.056	2776075.266	2891.775784	0.000814	0.000809	0.000824	0.007	0.002955	-0.001315	0.007711
9	GCP	32	1154358.606	2775977.916	2956.992188	1154358.605	2775977.916	2956.991055	0.000819	0.000821	0.000826	-0.000313	-0.000832	-0.001133	0.00144
11	GCP	13	1153891.238	2774914.615	2922.780273	1153891.233	2774914.611	2922.781795	0.000815	0.000817	0.000825	-0.003634	-0.004111	0.001522	0.005694
12	GCP	25	1153390.902	2775126.175	3050.238037	1153390.905	2775126.184	3050.240607	0.00081	0.000809	0.000821	0.008785	0.003062	0.00257	0.009652
13	GCP	15	1153484.757	2774483.773	2968.983643	1153484.758	2774483.769	2968.982008	0.000821	0.000823	0.000825	-0.003242	0.000663	-0.001635	0.003691
14	GCP	17	1153012.754	2775378.564	2963.132812	1153012.754	2775378.564	2963.132763	0.000816	0.000815	0.000824	0.000232	-0.000042	-0.00005	0.000241
Total GCP error												0.0056884	0.0109161	0.0080925	0.0147312
2	CP	31	1152361.15	2777465.86	2897.082031	1152361.241	2777465.622	2896.5102	0.005027	0.005813	0.007006	-0.238592	0.091088	-0.571831	0.62627
5	CP	19	1153115.838	2777088.093	2903.239502	1153115.489	2777088.142	2901.791667	0.013383	0.015026	0.018144	0.048827	-0.349027	-1.447834	1.49011
7	CP	48	1153157.659	2776087.66	2946.120117	1153157.72	2776088.479	2945.035009	0.00319	0.003193	0.00496	0.819376	0.060607	-1.085108	1.36107
10	CP	27	1154219.854	2775207.748	2895.315674	1154220.024	2775208.179	2895.653163	0.004862	0.004904	0.010394	0.431045	0.170453	0.337489	0.57337
15	CP	11	1152651.601	2775263.42	2920.831055	1152651.54	2775263.496	2920.134963	0.006472	0.006491	0.012926	0.075641	-0.061361	-0.696092	0.702873
Total error												0.429467	0.182543	0.916419	1.02839

https://doi.org/10.5194/essd-2026-194
Preprint. Discussion started: 4 May 2026

Open Access Earth System Science Data Discussions

850

Table B3: Ground control points (GCPs) and check points (CPs) used for high-resolution georeferencing of the Piz d'Err and Calderas DOM (model 3). Easting and northing given in the EPSG:2056 reference system.

Marker	Type	Images	Northing (y, m)	Easting (x, m)	Altitude (m)	Northing estimation (y, m)	Easting estimation (x, m)	Altitude estimation (m)	Northing variance (y, m)	Easting variance (x, m)	Altitude variance (m)	Error (x,m)	Error (y, m)	Error (z, m)	Error (xyz, m)
1	GCP	37	1157947.461	2771962.642	2718.968994	1157947.245	2771962.489	2718.418794	0.01349	0.013799	0.013434	-0.15267	-0.215786	-0.550201	0.610403
3	GCP	35	1157439.952	2772150.434	2962.105225	1157440.03	2772150.089	2962.487459	0.009835	0.010554	0.010116	-0.344244	0.078311	0.382234	0.520326
5	GCP	63	1157092.855	2772658.872	3177.033936	1157092.289	2772659.452	3177.090535	0.011594	0.012757	0.012064	0.580428	-0.566448	0.0566	0.812997
7	GCP	15	1156268.454	2771528.451	2539.569336	1156268.959	2771528.191	2539.969754	0.010928	0.011028	0.011693	-0.260119	0.505349	0.400418	0.695251
8	GCP	71	1155855.068	2771938.844	2867.796143	1155855.063	2771938.878	2867.509935	0.009525	0.009771	0.00953	0.033698	-0.004921	-0.286207	0.288226
9	GCP	66	1156103.951	2772924.261	3138.161865	1156104.011	2772924.093	3137.99213	0.014408	0.014481	0.014061	-0.167651	0.06042	-0.169735	0.246105
10	GCP	64	1154704.637	2773028.381	2956.460449	1154704.859	2773028.276	2956.700838	0.011279	0.012022	0.011888	-0.105232	0.221638	0.240389	0.343488
12	GCP	58	1155605.654	2771271.957	2600.174072	1155605.699	2771271.885	2599.995427	0.01247	0.012526	0.013231	-0.071308	0.04514	-0.178645	0.197577
14	GCP	11	1153485.96	2773059.34	2849.278076	1153486.256	2773058.648	2848.632104	0.014684	0.015074	0.014451	-0.692168	0.295356	-0.645972	0.991772
15	GCP	60	1154150.063	2773193.639	2990.245361	1154149.644	2773194.818	2990.996459	0.010655	0.012317	0.011236	1.179207	-0.419006	0.751098	1.459535
Total GCP error												0.496125	0.307664	0.423582	0.721262
2	CP	19	1157600.753	2771423.63	2538.610352	1157602.002	2771422.537	2538.057787	0.021281	0.019614	0.024642	-1.093311	1.249184	-0.552564	1.749605
4	CP	76	1156968.26	2771825.448	2684.228271	1156969.129	2771825.634	2680.413596	0.012171	0.013186	0.017874	0.18535	0.869689	-3.814676	3.916946
6	CP	34	1156526.686	2772237.149	2715.980469	1156527.662	2772236.604	2715.430194	0.01682	0.02336	0.019002	-0.544962	0.976917	-0.550275	1.246657
11	CP	26	1154726.73	2772330.277	2562.776123	1154724.129	2772333.647	2560.891793	0.050498	0.034574	0.034457	3.371255	-2.601919	-1.884329	4.656827
13	CP	5	1155433.047	2772786.737	2729.4729	1155435.591	2772786.636	2730.005222	0.024829	0.049107	0.07335	-0.101468	2.544713	0.532322	2.601773
Total error												1.60638	1.81751	1.94905	3.11169

855 **Table B4: Ground control points (GCPs) and check points (CPs) used for high-resolution georeferencing of the Piz d'Alp Val and Piz Bial DOM (model 4). Easting and northing given in the EPSG:2056 reference system.**

Marker	Type	Images	Northing (y, m)	Easting (x, m)	Altitude (m)	Northing estimation (y, m)	Easting estimation (x, m)	Altitude estimation (m)	Northing variance (y, m)	Easting variance (x, m)	Altitude variance (m)	Error (x,m)	Error (y, m)	Error (z, m)	Error (xyz, m)
2	GCP	15	1158781.958	2776877.351	2996.000244	1158781.953	2776877.348	2996.005558	0.000819	0.000826	0.000823	-0.003444	-0.005604	0.005314	0.008456
3	GCP	14	1158615.869	2777113.753	2953.849365	1158615.884	2777113.747	2953.840617	0.000793	0.0008	0.000811	-0.006133	0.015501	-0.008748	0.018826
5	GCP	29	1158942.965	2777338.839	2834.936279	1158942.97	2777338.844	2834.937237	0.000814	0.000811	0.00082	0.004902	0.004459	0.000958	0.006695
6	GCP	46	1158996.082	2777700.05	3022.502197	1158996.073	2777700.032	3022.498351	0.000813	0.000797	0.000813	-0.018793	-0.008999	-0.003846	0.021189
7	GCP	24	1158802.544	2777638.438	2993.5896	1158802.571	2777638.468	2993.609102	0.000767	0.000771	0.000789	0.030068	0.026677	0.019502	0.044678
8	GCP	17	1158634.737	2777627.063	2887.661133	1158634.713	2777627.044	2887.657127	0.000791	0.000785	0.000814	-0.018635	-0.023337	-0.004006	0.030131
10	GCP	16	1158237.777	2777405.464	2775.58252	1158237.788	2777405.466	2775.567565	0.000824	0.000815	0.000822	0.00211	0.011162	-0.014955	0.01878
13	GCP	27	1158231.156	2776874.232	2805.374756	1158231.157	2776874.233	2805.371974	0.000824	0.000823	0.000824	0.00117	0.000262	-0.002782	0.003029
12	GCP	28	1158293.95	2777086.564	2805.258057	1158293.938	2777086.561	2805.276896	0.000814	0.000807	0.000814	-0.003285	-0.012515	0.018839	0.022855
15	GCP	6	1158856.546	2777212.2	2896.743164	1158856.538	2777212.212	2896.732887	0.000825	0.000816	0.000822	0.01204	-0.007606	-0.010277	0.017563
Total GCP error												0.0135633	0.0140284	0.0109945	0.0223972
1	CP	18	1158725.751	2776638.15	2970.323975	1158725.463	2776638.679	2970.376894	0.025459	0.030598	0.02632	0.528908	-0.28812	0.05292	0.604614
9	CP	21	1158458.561	2777346.131	2839.934326	1158458.865	2777346.306	2840.053663	0.002365	0.002376	0.004335	0.174346	0.304691	0.119337	0.370775
4	CP	25	1158760.759	2777363.448	2916.659668	1158758.61	2777363.207	2919.202813	0.001933	0.002364	0.003365	-0.241094	-2.150218	2.543145	3.339035
11	CP	16	1158507.954	2776840.26	2879.708008	1158508.23	2776840.489	2880.09088	0.004142	0.008308	0.00652	0.229102	0.276061	0.382873	0.52468
14	CP	22	1158457.36	2776535.366	2866.997559	1158456.848	2776534.002	2866.529472	0.014976	0.011101	0.010349	-1.364779	-0.512554	-0.468087	1.531156
Total error												0.675777	1.01373	1.1705	1.68949

860

865

https://doi.org/10.5194/essd-2026-194
Preprint. Discussion started: 4 May 2026

Open Access Earth System Science Data Discussions

Table B5: Ground control points (GCPs) and check points (CPs) used for high-resolution georeferencing of the Fuorcla d'Agnel south DOM (model 5). Easting and northing given in the EPSG:2056 reference system.

Marker	Type	Images	Northing (y, m)	Easting (x, m)	Altitude (m)	Northing estimation (y, m)	Easting estimation (x, m)	Altitude estimation (m)	Northing variance (y, m)	Easting variance (x, m)	Altitude variance (m)	Error (x,m)	Error (y, m)	Error (z, m)	Error (xyz, m)
1	GCP	14	1153390.903	2775126.178	3050.238037	1153390.911	2775126.183	3050.260284	0.000802	0.000811	0.000799	0.005321	0.007696	0.022247	0.024134
3	GCP	23	1153410.066	2774835.221	3042.125244	1153410.053	2774835.219	3042.108789	0.00081	0.000813	0.000806	-0.002359	-0.012547	-0.016455	0.020827
5	GCP	12	1153402.298	2773850.104	2997.737549	1153402.29	2773850.113	2997.720328	0.000811	0.0008	0.000807	0.009086	-0.007245	-0.017221	0.020775
6	GCP	13	1153180.201	2773801.693	2901.006348	1153180.219	2773801.677	2901.030926	0.000806	0.000796	0.000804	-0.016083	0.017973	0.024578	0.034435
8	GCP	14	1152625.665	2773703.55	2826.03418	1152625.657	2773703.552	2826.033036	0.000808	0.000804	0.000803	0.002333	-0.007599	-0.001144	0.008031
9	GCP	19	1152218.951	2773589.463	2809.876953	1152218.952	2773589.467	2809.872674	0.000806	0.000804	0.000801	0.00364	0.000623	-0.004279	0.005653
11	GCP	12	1151730.251	2773248.947	2751.506592	1151730.25	2773248.947	2751.506359	0.000794	0.000803	0.0008	0.000043	-0.00017	-0.000233	0.000291
12	GCP	19	1151524.752	2773200.348	2738.953857	1151524.753	2773200.349	2738.95099	0.000789	0.000803	0.000787	0.000581	0.001338	-0.002867	0.003217
14	GCP	10	1151259.445	2773017.547	2690.198975	1151259.445	2773017.546	2690.201858	0.000814	0.000814	0.00081	-0.000904	-0.000587	0.002883	0.003078
15	GCP	10	1153465.744	2775354.453	3109.013916	1153465.745	2775354.451	3109.006407	0.000811	0.000815	0.000811	-0.001658	0.000519	-0.007509	0.007707
Total GCP error												0.0063064	0.00807925	0.0132623	0.0167611
2	CP	4	1153484.758	2774483.773	2968.983643	1153484.841	2774484.483	2969.546327	0.023029	0.009167	0.013857	0.711097	0.083062	0.562685	0.910589
4	CP	31	1153331.549	2774212.451	2973.803467	1153331.856	2774213.236	2974.017755	0.006906	0.004937	0.005924	0.7851	0.307379	0.214288	0.869933
7	CP	8	1152878.905	2773734.297	2853.797852	1152878.244	2773734.405	2853.250608	0.005398	0.007648	0.007489	0.107682	-0.660726	-0.547243	0.864656
10	CP	23	1151984.801	2773478.711	2734.720459	1151981.799	2773480.867	2731.227498	0.003837	0.00374	0.003593	2.157044	-3.003818	-3.49296	5.086898
13	CP	15	1151383.753	2773257.35	2747.704102	1151383.7	2773257.339	2747.599418	0.003685	0.003685	0.0045	-0.010451	-0.05335	-0.104683	0.117958
Total error												1.07579	1.38302	1.6046	2.37588

870

Table B6: Ground control points (GCPs) and check points (CPs) used for high-resolution georeferencing of the Fuorcla d'Agnel south north DOM (model 6). Easting and northing given in the EPSG:2056 reference system.

Marker	Type	Images	Northing (y, m)	Easting (x, m)	Altitude (m)	Northing estimation (y, m)	Easting estimation (x, m)	Altitude estimation (m)	Northing variance (y, m)	Easting variance (x, m)	Altitude variance (m)	Error (x,m)	Error (y, m)	Error (z, m)	Error (xyz, m)
3	GCP	17	1154071.368	2775111.408	2910.427002	1154071.37	2775111.405	2910.423228	0.000818	0.000819	0.000819	-0.002347	0.002333	-0.003774	0.005019
4	GCP	17	1154613.161	2774134.847	3002.426758	1154613.171	2774134.838	3002.448219	0.000805	0.000785	0.00078	-0.009625	0.010179	0.021461	0.025628
5	GCP	17	1153690.352	2774809.354	2938.854492	1153690.361	2774809.349	2938.842105	0.00081	0.000814	0.00081	-0.005145	0.009441	-0.012387	0.016403
6	GCP	16	1153688.972	2774519.887	2925.375244	1153688.938	2774519.921	2925.423566	0.000802	0.000801	0.000796	0.033615	-0.033984	0.048321	0.067969
7	GCP	23	1153601.176	2774217.063	3017.828857	1153601.21	2774217.035	3017.779599	0.000808	0.000803	0.00079	-0.027783	0.034052	-0.049259	0.066014
8	GCP	22	1153650.572	2773840.467	3018.866943	1153650.559	2773840.469	3018.884382	0.000816	0.000816	0.000813	0.001482	-0.013038	0.017438	0.021824
9	GCP	28	1154227.458	2773720.256	3058.04248	1154227.468	2773720.262	3058.041774	0.000808	0.000817	0.000813	0.00582	0.009444	-0.000707	0.011116
10	GCP	26	1154362.862	2773986.137	2974.001465	1154362.834	2773986.132	2973.980138	0.000796	0.0008	0.00079	-0.005666	-0.02843	-0.021327	0.035989
11	GCP	36	1154732.647	2774104.194	3064.896973	1154732.66	2774104.204	3064.919909	0.000804	0.000785	0.000791	0.00996	0.012927	0.022936	0.028149
13	GCP	16	1154906.042	2774203.443	3231.526123	1154906.04	2774203.443	3231.50342	0.000815	0.000815	0.000812	-0.000311	-0.002924	-0.022703	0.022893
Total GCP error												0.0148119	0.0193797	0.0268152	0.0362494
1	CP	13	1154219.864	2775207.764	2895.315674	1154220.87	2775210.879	2895.602976	0.007433	0.013102	0.005898	3.116349	1.00717	0.287303	3.287638
2	CP	18	1153891.233	2774914.614	2922.780273	1153890.932	2774915.924	2923.602445	0.00391	0.006837	0.005471	1.310606	-0.300986	0.822172	1.576149
12	CP	11	1154606.181	2774389.814	2928.436279	1154606.626	2774389.467	2929.881202	0.006302	0.004522	0.007434	-0.347491	0.445659	1.444922	1.551503
14	CP	12	1155126.256	2774454.916	3016.691406	1155127.464	2774456.334	3020.076704	0.014769	0.012692	0.008653	1.418559	1.208369	3.385298	3.864286
15	CP	22	1155228.55	2774719.238	2911.631104	1155228.698	2774721.479	2914.834583	0.024171	0.018338	0.017453	2.241875	0.148173	3.203479	3.91283
Total error												1.92813	0.746419	2.2167	3.03127

875

880

https://doi.org/10.5194/essd-2026-194
Preprint. Discussion started: 4 May 2026

Open Access Earth System Science Data Discussions

Table B7: Ground control points (GCPs) and check points (CPs) used for high-resolution georeferencing of the Piz Jenatsch south 1 DOM (model 7). Easting and northing given in the EPSG:2056 reference system.

Marker	Type	Images	Northing (y, m)	Easting (x, m)	Altitude (m)	Northing estimation (y, m)	Easting estimation (x, m)	Altitude estimation (m)	Northing variance (y, m)	Easting variance (x, m)	Altitude variance (m)	Error (x,m)	Error (y, m)	Error (z, m)	Error (xyz, m)
1	GCP	7	1156043.653	2773444.659	3140.463379	1156043.654	2773444.66	3140.463042	0.000704	0.000709	0.000707	0.00151	0.001051	-0.000337	0.00187
2	GCP	40	1156805.142	2774929.158	3014.034912	1156805.148	2774929.158	3014.043352	0.000711	0.000711	0.00071	0.00024	0.005647	0.00844	0.010157
4	GCP	34	1157037.235	2774153.541	3012.124756	1157037.222	2774153.54	3012.105791	0.000705	0.000709	0.000705	-0.001462	-0.013372	-0.018965	0.023251
6	GCP	13	1157048.365	2773468.473	3117.57666	1157048.382	2773468.467	3117.598983	0.000704	0.000704	0.000704	-0.006337	0.016594	0.022323	0.028527
7	GCP	42	1157001.557	2773028.141	3242.463867	1157001.557	2773028.145	3242.456202	0.000707	0.000708	0.000707	0.00441	0.000494	-0.007665	0.008857
8	GCP	12	1155555.726	2773940.021	2955.800049	1155555.725	2773940.016	2955.810024	0.000707	0.000707	0.000706	-0.004779	-0.001724	0.009976	0.011195
10	GCP	43	1156411.283	2774062.66	2895.015625	1156411.261	2774062.646	2895.033664	0.00069	0.0007	0.000702	-0.014051	-0.021785	0.018039	0.031582
12	GCP	27	1156007.664	2773968.253	2884.541992	1156007.669	2773968.272	2884.519506	0.000695	0.000699	0.000693	0.01969	0.004884	-0.022486	0.030285
13	GCP	9	1155915.855	2774483.267	2841.493896	1155915.867	2774483.27	2841.478118	0.000705	0.000705	0.000703	0.003077	0.012475	-0.015778	0.020348
15	GCP	20	1155404.409	2774892.048	2724.055908	1155404.404	2774892.045	2724.062364	0.00071	0.00071	0.000709	-0.002297	-0.004263	0.006456	0.00807
Total GCP error												0.0082873	0.0107825	0.0148635	0.0201461
3	CP	71	1156960.156	2774612.978	3067.934082	1156960.431	2774613.077	3067.876294	0.003944	0.002782	0.003799	0.099381	0.27455	-0.057788	0.297648
5	CP	19	1155602.314	2774379.419	2871.783447	1155602.37	2774379.765	2872.153806	0.007061	0.00487	0.005661	0.346522	0.05584	0.370359	0.510256
9	CP	16	1156729.197	2773782.125	2921.921143	1156729.14	2773782.147	2922.036921	0.003094	0.003289	0.005476	0.021912	-0.057042	0.115779	0.130915
11	CP	11	1156203.148	2773604.197	3227.54834	1156203.378	2773604.483	3227.578933	0.003088	0.006443	0.005512	0.286075	0.230668	0.030593	0.368759
14	CP	18	1155712.449	2774686.212	2870.10791	1155712.303	2774686.798	2870.698002	0.004634	0.007776	0.005285	0.586551	-0.145542	0.590091	0.844649
Total error												0.333561	0.176715	0.317192	0.493054

885

Table B8: Ground control points (GCPs) and check points (CPs) used for high-resolution georeferencing of the Piz Jenatsch south 2 DOM (model 8). Easting and northing given in the EPSG:2056 reference system.

Marker	Type	Images	Northing (y, m)	Easting (x, m)	Altitude (m)	Northing estimation (y, m)	Easting estimation (x, m)	Altitude estimation (m)	Northing variance (y, m)	Easting variance (x, m)	Altitude variance (m)	Error (x,m)	Error (y, m)	Error (z, m)	Error (xyz, m)
1	GCP	16	1156240.659	2775144.242	2847.706299	1156240.674	2775144.228	2847.714548	0.000822	0.000818	0.000799	-0.014191	0.014502	0.008249	0.021903
3	GCP	13	1156356.649	2774991.329	2831.21167	1156356.644	2774991.331	2831.204098	0.000821	0.000809	0.000794	0.001861	-0.005013	-0.007572	0.009269
5	GCP	16	1156430.775	2775052.322	2911.376221	1156430.767	2775052.329	2911.355992	0.000821	0.000801	0.000795	0.006736	-0.007989	-0.020228	0.022768
7	GCP	12	1156561.254	2774552.541	2912.988281	1156561.256	2774552.542	2912.990099	0.000834	0.00083	0.000832	0.00072	0.001254	0.001818	0.002322
8	GCP	16	1156662.851	2774836.857	2953.14209	1156662.852	2774836.852	2953.148378	0.000832	0.000823	0.000824	-0.004725	0.001024	0.006288	0.007932
9	GCP	7	1156250.421	2775314.774	2889.776367	1156250.415	2775314.786	2889.797669	0.000826	0.000824	0.000814	0.01202	-0.005408	0.021301	0.02505
10	GCP	8	1156150.98	2775478.161	2889.907227	1156150.982	2775478.159	2889.897371	0.00083	0.000833	0.000828	-0.002421	0.001631	-0.009856	0.010279
Total GCP error												0.0077774	0.00690522	0.0126959	0.016412
2	CP	7	1156068.154	2775354.744	2849.848145	1156068.581	2775354.692	2849.734938	0.008586	0.017141	0.007226	-0.052327	0.426814	-0.113207	0.444661
4	CP	11	1156396.867	2774790.858	2835.514404	1156396.702	2774790.615	2835.618755	0.006336	0.004014	0.003337	-0.242841	-0.165143	0.104351	0.311662
6	CP	11	1156491.875	2774390.733	2870.272461	1156491.422	2774391.058	2871.640687	0.013557	0.006333	0.00513	0.324871	-0.453267	1.368226	1.47751
Total CP error												0.236115	0.371884	0.794931	0.908826

890

895

https://doi.org/10.5194/essd-2026-194
Preprint. Discussion started: 4 May 2026

Open Access Earth System Science Data Discussions

900

Table B9: Ground control points (GCPs) and check points (CPs) used for high-resolution georeferencing of the Corn Alv DOM (model 9). Easting and northing given in the EPSG:2056 reference system.

Marker	Type	Images	Northing (y, m)	Easting (x, m)	Altitude (m)	Northing estimation (y, m)	Easting estimation (x, m)	Altitude estimation (m)	Northing variance (y, m)	Easting variance (x, m)	Altitude variance (m)	Error (x,m)	Error (y, m)	Error (z, m)	Error (xyz, m)
1	GCP	17	1153012.754	2775378.564	2963.132812	1153012.757	2775378.563	2963.129592	0.000725	0.000728	0.000726	-0.000997	0.002066	-0.00322	0.003954
3	GCP	21	1152342.939	2775271.943	2882.006592	1152342.947	2775271.956	2882.027487	0.000714	0.000723	0.000718	0.012443	0.007506	0.020895	0.025451
5	GCP	26	1152355.41	2774790.166	2783.12793	1152355.388	2774790.163	2783.115033	0.000705	0.000705	0.00072	-0.00272	-0.022472	-0.012897	0.026052
6	GCP	31	1152906.168	2774867.343	2865.520508	1152906.164	2774867.344	2865.514921	0.000723	0.000709	0.000717	0.000861	-0.004056	-0.005587	0.006957
8	GCP	24	1152014.45	2774999.541	2836.843506	1152014.443	2774999.526	2836.826723	0.000683	0.000693	0.000706	-0.014766	-0.007076	-0.016783	0.023447
10	GCP	26	1151457.724	2774560.36	2683.355469	1151457.718	2774560.361	2683.363279	0.000726	0.00072	0.000726	0.001374	-0.00604	0.00781	0.009968
12	GCP	24	1151868.466	2774805.347	2827.529053	1151868.481	2774805.345	2827.528321	0.000697	0.000695	0.00071	-0.002524	0.015182	-0.000732	0.015408
13	GCP	28	1151245.356	2775479.143	2675.798828	1151245.353	2775479.137	2675.787018	0.000724	0.000727	0.000723	-0.005785	-0.002949	-0.01181	0.013478
14	GCP	32	1151411.09	2775607.963	2724.108643	1151411.098	2775607.969	2724.117934	0.000723	0.000728	0.000723	0.005629	0.007537	0.009291	0.013222
15	GCP	27	1152618.447	2774665.756	2766.673828	1152618.457	2774665.763	2766.686861	0.000719	0.000709	0.000714	0.006485	0.010303	0.013033	0.017834
Total GCP error												0.0070529	0.0103477	0.0117618	0.0171802
2	CP	9	1152657.34	2775262.886	2921.094727	1152658.595	2775264.139	2919.72083	0.028361	0.018679	0.013175	1.253329	1.256125	-1.373896	2.244164
4	CP	54	1152570.374	2774892.845	2791.305664	1152570.316	2774892.834	2791.106933	0.002773	0.001916	0.002808	-0.011694	-0.058607	-0.198731	0.207523
7	CP	15	1152264.205	2775050.097	2798.94458	1152263.994	2775049.861	2798.790226	0.001804	0.002868	0.005059	-0.236278	-0.211187	-0.154354	0.352494
9	CP	32	1151778.446	2774600.031	2733.14502	1151778.5	2774599.718	2732.852114	0.002414	0.002542	0.004427	-0.31293	0.05449	-0.292905	0.432073
11	CP	31	1151012.979	2775230.545	2615.956543	1151013.03	2775230.387	2615.272738	0.022053	0.022984	0.013279	-0.158481	0.050685	-0.683805	0.703757
Total error												0.591581	0.571213	0.707713	1.08495

905 **Table B10: Ground control points (GCPs) and check points (CPs) used for high-resolution georeferencing of the Pir Neir DOM (model 10). Easting and northing given in the EPSG:2056 reference system.**

Marker	Type	Images	Northing (y, m)	Easting (x, m)	Altitude (m)	Northing estimation (y, m)	Easting estimation (x, m)	Altitude estimation (m)	Northing variance (y, m)	Easting variance (x, m)	Altitude variance (m)	Error (x,m)	Error (y, m)	Error (z, m)	Error (xyz, m)
2	GCP	30	1149974.659	2772294.153	2556.747803	1149974.646	2772294.149	2556.748139	0.000744	0.000741	0.000743	-0.004442	-0.01326	0.000336	0.013988
4	GCP	34	1150361.554	2772302.247	2700.248535	1150361.556	2772302.254	2700.237521	0.000748	0.000736	0.000728	0.007013	0.001656	-0.011014	0.013162
6	GCP	25	1150727.261	2772429.342	2710.435059	1150727.271	2772429.339	2710.43369	0.00072	0.000737	0.000723	-0.0034	0.009673	-0.001369	0.010344
7	GCP	47	1150616.969	2772780.153	2625.47168	1150616.995	2772780.133	2625.516223	0.000711	0.000705	0.000702	-0.01982	0.026089	0.044543	0.055295
9	GCP	14	1150714.756	2773130.945	2644.179688	1150714.741	2773130.958	2644.159916	0.000739	0.000728	0.000721	0.013601	-0.014844	-0.019772	0.028218
10	GCP	35	1150622.458	2773585.149	2630.208984	1150622.46	2773585.146	2630.203542	0.000735	0.000748	0.00074	-0.003173	0.00166	-0.005442	0.006515
11	GCP	66	1150679.26	2772164.761	2778.828369	1150679.252	2772164.772	2778.822897	0.000721	0.000741	0.000727	0.010823	-0.00804	-0.005472	0.014551
13	GCP	22	1151261.205	2772874.296	2704.253906	1151261.205	2772874.299	2704.25495	0.00075	0.000744	0.000743	0.003387	-0.000587	0.001043	0.003592
14	GCP	29	1150878.173	2772964.33	2710.862061	1150878.169	2772964.323	2710.85088	0.000744	0.000698	0.000709	-0.00693	-0.003923	-0.011181	0.013727
15	GCP	17	1150866.265	2773553.344	2623.775879	1150866.266	2773553.347	2623.784207	0.000744	0.000744	0.000741	0.00294	0.001577	0.008328	0.008971
Total GCP error												0.0092392	0.0112193	0.0165932	0.0.20583
1	CP	24	1149673.463	2772523.495	2416.48877	1149673.179	2772523.789	2416.678492	0.006155	0.010011	0.006481	0.294379	-0.284471	0.189722	0.451195
3	CP	55	1150083.751	2771971.148	2660.998535	1150084.337	2771971.414	2661.953826	0.00352	0.003561	0.002822	0.266471	0.586072	0.955291	1.151984
5	CP	92	1150277.345	2772640.552	2608.998291	1150277.536	2772640.79	2608.731548	0.002229	0.002354	0.001902	0.238156	0.190235	-0.266743	0.405043
8	CP	41	1150831.044	2772775.352	2713.935791	1150831.111	2772775.359	2714.068056	0.002638	0.001693	0.001829	0.006875	0.066961	0.132265	0.148409
12	CP	40	1151545	2772975.223	2702.101562	1151545.646	2772975.606	2702.557202	0.014772	0.005387	0.005159	0.382985	0.646082	0.45564	0.878469
Total error												0.268741	0.420119	0.498965	0.70547

910

915

https://doi.org/10.5194/essd-2026-194
Preprint. Discussion started: 4 May 2026

Open Access Earth System Science Data Discussions

Table B11: Ground control points (GCPs) and check points (CPs) used for high-resolution georeferencing of the Laviner and Jenatsch area DOM (model 11). Easting and northing given in the EPSG:2056 reference system.

Marker	Type	Images	Northing (y, m)	Easting (x, m)	Altitude (m)	Northing estimation (y, m)	Easting estimation (x, m)	Altitude estimation (m)	Northing variance (y, m)	Easting variance (x, m)	Altitude variance (m)	Error (x,m)	Error (y, m)	Error (z, m)	Error (xyz, m)
1	GCP	104	1158003.25	2775452.851	3130.38916	1158003.22	2775452.575	3130.534484	0.016566	0.016664	0.016939	-0.276621	-0.030629	0.145324	0.313969
2	GCP	83	1157718.95	2776269.463	2933.107666	1157718.567	2776269.455	2933.176179	0.022782	0.022639	0.027541	-0.008394	-0.38303	0.068513	0.3892
4	GCP	50	1156819.255	2775527.762	2879.80127	1156819.449	2775527.972	2878.96781	0.01873	0.018998	0.023801	0.20987	0.194294	-0.833459	0.881164
5	GCP	49	1156661.498	2774834.305	2952.876221	1156661.507	2774834.384	2953.497763	0.019989	0.021656	0.021595	0.079523	0.009487	0.621542	0.62668
6	GCP	13	1158766.733	2775472.563	2947.176758	1158767.308	2775472.64	2947.0621	0.027592	0.026512	0.030607	0.07675	0.574574	-0.114657	0.590908
8	GCP	77	1156805.142	2774929.158	3014.034912	1156805.237	2774929.095	3014.694282	0.017894	0.019241	0.019007	-0.06312	0.095049	0.65937	0.669169
10	GCP	28	1157037.235	2774153.541	3012.124756	1157037.417	2774153.997	3011.459236	0.031308	0.030583	0.029801	0.455331	0.181865	-0.66552	0.82663
11	GCP	42	1157889.557	2775960.571	2967.312256	1157889.448	2775960.647	2967.032137	0.018432	0.018163	0.020408	0.07661	-0.108303	-0.280119	0.309944
13	GCP	24	1157809.761	2775216.363	3029.088135	1157809.481	2775216.012	3029.749731	0.015528	0.015503	0.016419	-0.351387	-0.280749	0.661596	0.800001
15	GCP	21	1157322.15	2775042.944	2940.967529	1157321.898	2775042.746	2940.704919	0.015849	0.016672	0.015897	-0.198551	-0.252555	-0.262611	0.414935
Total GCP error												0.226478	0.266846	0.508208	0.617069
3	CP	94	1157345.051	2775500.264	2861.72583	1157344.735	2775499.812	2861.515581	0.016302	0.015088	0.016262	-0.452108	-0.316132	-0.210249	0.590377
7	CP	17	1157295.252	2773979.951	3041.844238	1157295.619	2773981.395	3042.999332	0.047253	0.049217	0.050022	1.444191	0.366932	1.155094	1.885356
9	CP	57	1156960.156	2774612.978	3067.934082	1156959.602	2774613.351	3068.218208	0.02122	0.021506	0.020968	0.373486	-0.554499	0.284126	0.726421
12	CP	17	1158246.458	2775403.144	3033.013184	1158246.644	2775402.794	3033.309877	0.018736	0.019301	0.021608	-0.349445	0.185898	0.296693	0.494668
14	CP	38	1156430.142	2775873.556	2932.576416	1156429.8	2775872.168	2932.646514	0.0258	0.027408	0.038356	-1.389113	-0.342326	0.070098	1.432388
Total CP error												0.946713	0.372503	0.557156	1.15993

920

Table B12: Ground control points (GCPs) and check points (CPs) used for high-resolution georeferencing of the Val da Fain DOM (model 12). Easting and northing given in the EPSG:2056 reference system.

Marker	Type	Images	Northing (y, m)	Easting (x, m)	Altitude (m)	Northing estimation (y, m)	Easting estimation (x, m)	Altitude estimation (m)	Northing variance (y, m)	Easting variance (x, m)	Altitude variance (m)	Error (x,m)	Error (y, m)	Error (z, m)	Error (xyz, m)
1	GCP	65	1149616.061	2796159.855	2641.076904	1149616.101	2796159.868	2641.075148	0.00079	0.00079	0.000792	0.012642	0.039715	-0.001756	0.041716
2	GCP	96	1149950.346	2797441.658	2687.354492	1149950.343	2797441.639	2687.365469	0.000789	0.000782	0.000788	-0.019503	-0.002934	0.010976	0.022571
4	GCP	67	1148413.155	2797624.544	2537.53418	1148413.165	2797624.564	2537.537866	0.00079	0.000789	0.000789	0.019986	0.010615	0.003687	0.022928
5	GCP	59	1146972.457	2796318.84	2507.528076	1146972.469	2796318.858	2507.534961	0.00079	0.000792	0.000791	0.018416	0.011985	0.006885	0.023026
6	GCP	24	1149442.339	2794964.748	2802.346924	1149442.349	2794964.75	2802.352626	0.000793	0.000793	0.000793	0.002315	0.009629	0.005702	0.011427
8	GCP	18	1150127.248	2796421.346	2757.806641	1150127.157	2796421.341	2757.798019	0.000791	0.000786	0.000792	-0.005361	-0.090743	-0.008621	0.091309
10	GCP	32	1149865.803	2798095.288	2546.57251	1149865.802	2798095.343	2546.548423	0.00079	0.000787	0.000789	0.055405	-0.001036	-0.024087	0.060424
11	GCP	16	1149118.245	2798416.663	2484.601807	1149118.299	2798416.64	2484.615691	0.00079	0.000791	0.000791	-0.022521	0.053279	0.013884	0.059486
13	GCP	90	1148038.964	2796985.346	2597.172852	1148038.997	2796985.327	2597.167728	0.000789	0.000788	0.00079	-0.018268	0.033389	-0.005124	0.038403
15	GCP	23	1147118.142	2796865.539	2699.858643	1147118.078	2796865.495	2699.857097	0.00079	0.000791	0.000791	-0.04311	-0.063895	-0.001545	0.077094
Total GCP error												0.0266121	0.0426688	0.0104546	0.0513627
3	CP	12	1149545.284	2798581.384	2434.057129	1149545.37	2798580.939	2434.645846	0.02135	0.055886	0.045451	-0.445884	0.086266	0.588717	0.743534
7	CP	13	1149251.353	2795496.351	2552.212402	1149250.985	2795497.028	2551.948002	0.033882	0.03624	0.051906	0.677393	-0.368237	-0.264401	0.815088
9	CP	62	1149670.64	2796898.154	2649.309814	1149670.848	2796898.373	2649.084504	0.004879	0.003634	0.006019	0.219391	0.207926	-0.225311	0.377002
12	CP	31	1148787.058	2798104.956	2519.486816	1148787.045	2798104.994	2519.416327	0.007827	0.007542	0.009667	0.037842	-0.012482	-0.07049	0.080973
14	CP	70	1147786.76	2796443.85	2506.299072	1147786.863	2796443.747	2506.385971	0.005714	0.005905	0.00739	-0.103101	0.102522	0.086899	0.169387
Total error												0.378911	0.198464	0.309768	0.528127